LOFAR Detection of 110–188 MHz Emission and Frequency-Dependent Activity from FRB 20180916B

Z. Pleunis,[1, 2] D. Michilli,[1, 2] C. G. Bassa,[3] J. W. T. Hessels,[3, 4] A. Naidu,[5] B. C. Andersen,[1, 2] P. Chawla,[1, 2]
E. Fonseca,[1, 2, 6, 7] V. M. Kaspi,[1, 2] D. Z. Li,[8, 9] M. Bhardwaj,[1, 2] P. J. Boyle,[1, 2] C. Brar,[1, 2] T. Cassanelli,[10, 11]
A. Gopinath,[3, 4] Y. Gupta,[12] A. Josephy,[1, 2] R. Karuppusamy,[13] A. Keimpema,[14] F. Kirsten,[15] V. I. Kondratiev,[3, 16]
C. Leung,[17, 18] B. Marcote,[14] K. Masui,[17, 18] R. Mckinven,[10, 11] B. W. Meyers,[19] C. Ng,[10] K. Nimmo,[3, 4] Z. Paragi,[14]
M. Rahman,[10, 20] P. Scholz,[10] K. Shin,[17, 18] K. M. Smith,[21] I. H. Stairs,[19] and S. P. Tendulkar[22, 12]

[1] Department of Physics, McGill University, 3600 rue University, Montréal, QC H3A 2T8, Canada
[2] McGill Space Institute, McGill University, 3550 rue University, Montréal, QC H3A 2A7, Canada
[3] ASTRON, The Netherlands Institute for Radio Astronomy, Oude Hoogeveensedijk 4, 7991 PD Dwingeloo, The Netherlands
[4] Anton Pannekoek Institute for Astronomy, University of Amsterdam, Science Park 904, 1098 XH Amsterdam, The Netherlands
[5] University of Oxford, Sub-Department of Astrophysics, Denys Wilkinson Building, Keble Road, Oxford, OX1 3RH, United Kingdom
[6] Department of Physics and Astronomy, West Virginia University, P.O. Box 6315, Morgantown, WV 26506, USA
[7] Center for Gravitational Waves and Cosmology, West Virginia University, Chestnut Ridge Research Building, Morgantown, WV 26505,
USA
[8] Department of Physics, University of Toronto, 60 St. George Street, Toronto, ON M5S 1A7, Canada
[9] Canadian Institute for Theoretical Astrophysics, 60 St. George Street, Toronto, ON M5S 3H8, Canada
[10] Dunlap Institute for Astronomy & Astrophysics, University of Toronto, 50 St. George Street, Toronto, ON M5S 3H4, Canada
[11] David A. Dunlap Department of Astronomy & Astrophysics, University of Toronto, 50 St. George Street, Toronto, ON M5S 3H4,
Canada
[12] National Centre for Radio Astrophysics, Post Bag 3, Ganeshkhind, Pune, 411007, India
[13] Max Planck Institute for Radio Astronomy, Auf dem Hügel 69, 53121 Bonn, Germany
[14] Joint Institute for VLBI ERIC, Oude Hoogeveensedijk 4, 7991PD Dwingeloo, The Netherlands
[15] Department of Space, Earth and Environment, Chalmers University of Technology, Onsala Space Observatory, 439 92, Onsala, Sweden
[16] Astro Space Centre, Lebedev Physical Institute, Russian Academy of Sciences, Profsoyuznaya Str. 84/32, Moscow 117997, Russia
[17] MIT Kavli Institute for Astrophysics and Space Research, Massachusetts Institute of Technology, 77 Massachusetts Ave, Cambridge,
MA 02139, USA
[18] Department of Physics, Massachusetts Institute of Technology, 77 Massachusetts Ave, Cambridge, MA 02139, USA
[19] Dept. of Physics and Astronomy, 6224 Agricultural Road, Vancouver, BC V6T 1Z1 Canada
[20] Sidrat Research, PO Box 73527 RPO Wychwood, Toronto, Ontario, M6C 4A7, Canada
[21] Perimeter Institute for Theoretical Physics, 31 Caroline Street N, Waterloo ON N2L 2Y5 Canada
[22] Department of Astronomy and Astrophysics, Tata Institute of Fundamental Research, Mumbai, 400005, India

ABSTRACT

FRB 20180916B is a well-studied repeating fast radio burst source. Its proximity ($\sim 150\,\mathrm{Mpc}$), along with detailed studies of the bursts, have revealed many clues about its nature — including a 16.3-day periodicity in its activity. Here we report on the detection of 18 bursts using LOFAR at 110–188 MHz, by far the lowest-frequency detections of any FRB to date. Some bursts are seen down to the lowest-observed frequency of 110 MHz, suggesting that their spectra extend even lower. These observations provide an order-of-magnitude stronger constraint on the optical depth due to free-free absorption in the source's local environment. The absence of circular polarization and nearly flat polarization angle curves are consistent with burst properties seen at $300 - 1700\,\mathrm{MHz}$. Compared with higher frequencies, the larger burst widths ($\sim 40 - 160\,\mathrm{ms}$ at $150\,\mathrm{MHz}$) and lower linear polarization fractions are likely due to scattering. We find $\sim 2 - 3\,\mathrm{rad\ m^{-2}}$ variations in the Faraday rotation measure that may

Corresponding author: Ziggy Pleunis
ziggy.pleunis@physics.mcgill.ca

be correlated with the activity cycle of the source. We compare the LOFAR burst arrival times to those of 38 previously published and 22 newly detected bursts from the uGMRT ($200 - 450\,\mathrm{MHz}$) and CHIME/FRB ($400 - 800\,\mathrm{MHz}$). Simultaneous observations show 5 CHIME/FRB bursts when no emission is detected by LOFAR. We find that the burst activity is systematically delayed towards lower frequencies by ∼three days from $600\,\mathrm{MHz}$ to $150\,\mathrm{MHz}$. We discuss these results in the context of a model in which FRB 20180916B is an interacting binary system featuring a neutron star and high-mass stellar companion.

1. INTRODUCTION

The discovery of radio pulsars (Hewish et al. 1968) using a low-frequency dipole array ($81.5\,\mathrm{MHz}$) established the existence of neutron stars, and demonstrated that short-duration, coherent radio pulses can be the sirens of extreme astrophysical environments and events. The prediction of coherent radio bursts from other extreme astrophysical settings and events (e.g., Colgate & Noerdlinger 1971) inspired early searches for fast radio transients using archival pulsar survey data (e.g., Phinney & Taylor 1979). The discovery of the 'Lorimer Burst' (Lorimer et al. 2007) in archival Parkes pulsar survey data led to the establishment of a population of fast radio bursts (FRBs).

FRBs are sub-second radio flashes that can be detected over extragalactic distances (see Petroff et al. 2019 and Cordes & Chatterjee 2019 for recent reviews). Their physical origin is as yet unclear, but dozens of models have been proposed (see Platts et al. 2019, for a catalog[1] of theories). Both repeating (Spitler et al. 2016) and apparently non-repeating (Petroff et al. 2015; Shannon et al. 2018) FRBs have been detected, and could potentially be created by physically distinct sources or emission mechanisms (CHIME/FRB Collaboration et al. 2019a; Fonseca et al. 2020). Because of their short duration and high brightness temperature, many models have invoked compact objects as the source of FRBs. The recent discovery of an extremely luminous radio burst from the Galactic magnetar SGR J1935+2154 (CHIME/FRB Collaboration et al. 2020b; Bochenek et al. 2020) strengthens the case for FRB models that invoke a similar type of source. In any case, SGR J1935+2154 has demonstrated that neutron stars can produce millisecond-duration radio flashes spanning over seven orders-of-magnitude in apparent luminosity (Kirsten et al. 2020).

[1] https://frbtheorycat.org/

The lack of prompt optical, X-ray or gamma-ray counterparts to FRBs[2] (Scholz et al. 2017, 2020; Hardy et al. 2017) underscores the need to extract as many useful constraints as possible from the properties of the radio bursts themselves. Fortunately, detailed spectro-temporal and polarimetric studies of FRBs — using raw voltage data where possible — provide important insights into the emission mechanism and local environment (e.g., Farah et al. 2018; Cho et al. 2020; Day et al. 2020; Nimmo et al. 2020). These studies reveal, e.g, that viable emission mechanisms must account for a wide dynamic range of timescales within and between bursts: from a few microseconds up to several milliseconds (Nimmo et al. 2020). The frequency drifts of sub-bursts (i.e., the 'sad trombone' effect; Hessels et al. 2019) appear to be a common feature of repeaters (CHIME/FRB Collaboration et al. 2019b). While some repeating FRBs show remarkably similar polarimetric properties — e.g., FRB 20121102A and FRB 20180916B show flat polarization position angle within and *between* bursts (Michilli et al. 2018; Nimmo et al. 2020) — the repeating FRB 180301 shows diverse polarization angle swings between bursts (Luo et al. 2020). A larger sample is needed for confirmation, but these spectro-temporal and polarimetric characteristics may indicate a different physical origin or emission mechanism compared to apparent non-repeaters.

Along with FRB 20121102A, FRB 20180916B discovered by the Canadian Hydrogen Intensity Mapping Experiment FRB backend (CHIME/FRB; CHIME/FRB Collaboration et al. 2019a), is the best-characterized repeating FRB. It has recently been shown that the burst rate of FRB 20180916B varies with a period of $16.35 \pm 0.15\,\mathrm{days}$ (CHIME/FRB Collaboration et al. 2020a, hereafter PR3). FRB 20121102A may also have a ∼ 160-day period to its activity (Rajwade et al. 2020; Cruces et al. 2021). These activity periods might reflect an orbital period (Ioka & Zhang 2020; Lyutikov et al. 2020; Zhang & Gao 2020; Popov 2020), rotational pe-

[2] Though note that the Galactic event from SGR 1935+2154 was accompanied by a hard X-ray burst (Mereghetti et al. 2020).

riod (Beniamini et al. 2020), or precession period (Levin et al. 2020; Sob'yanin 2020; Yang & Zou 2020; Zanazzi & Lai 2020).

FRB 20180916B is located in a spiral galaxy at a luminosity distance of $D_{\mathrm{L}} = 149\,\mathrm{Mpc}$ (Marcote et al. 2020). This distance makes FRB 20180916B by far the closest known FRB source with a precise localization; in fact, it is also the most precisely localized FRB to date. The 2.3-mas localization provided by the European Very-long-baseline interferometry Network (EVN; Marcote et al. 2020), coupled with $60 - 90$-mas imaging from the *Hubble Space Telescope* (*HST*), demonstrates that FRB 20180916B is close to, but still offset by $\sim 250\,\mathrm{pc}$ from the nearest knot of star formation in the host galaxy (Tendulkar et al. 2020). This suggests that FRB 20180916B may be too old ($100\,\mathrm{kyr}-10\,\mathrm{Myr}$) to host an active magnetar. Rather, Tendulkar et al. (2020) argue that FRB 20180916B may be a high-mass X-ray binary (HMXB) where interaction between the companion wind and neutron-star magnetosphere produces FRBs.

To date, FRBs have been detected from radio frequencies of $300\,\mathrm{MHz}$ (Chawla et al. 2020; Pilia et al. 2020; Parent et al. 2020) up to $8\,\mathrm{GHz}$ (Gajjar et al. 2018). FRB 20180916B has thus far only been detected up to $1.7\,\mathrm{GHz}$ (Marcote et al. 2020), and Pearlman et al. (2020) demonstrate that it is either less active or fainter at higher frequencies ($\gtrsim 2\,\mathrm{GHz}$). In simultaneous Low-Frequency Array (LOFAR) and Green Bank Telescope (GBT) observations, Chawla et al. (2020) demonstrate burst detections at $300 - 400\,\mathrm{MHz}$, while no emission is seen contemporaneously at $110 - 188\,\mathrm{MHz}$. Likewise, Pearlman et al. (2020) use Deep Space Network 70-m dish observations to demonstrate that no emission is detected at $2.3\,\mathrm{GHz}$ or $8.4\,\mathrm{GHz}$ at the time of a bright burst seen by CHIME/FRB from $600 - 800\,\mathrm{MHz}$. Such narrow-band emission appears to be a characteristic of repeating FRBs (e.g., Kumar et al. 2021), and has also been well demonstrated for FRB 20121102A (Gourdji et al. 2019; Majid et al. 2020).

Detecting FRBs at very low radio frequencies ($< 300\,\mathrm{MHz}$) is challenging: sky background temperature (T_{sky}), scattering in the intervening ionized medium, and uncorrected intra-channel dispersive smearing can all reduce the observed signal-to-noise ratio (S/N). Nonetheless, low-frequency searches can provide strong constraints on the emission mechanism and local environment of an FRB, e.g., by quantifying the influence of free-free absorption, where the optical depth scales roughly quadratically with radio frequency, $\tau_{\mathrm{ff}} \propto \nu^{-2.1}$. Low-frequency FRB searches are thus well motivated scientifically, despite the increased observational chal-lenges. More than 50 years after the seminal discovery of radio pulsars, we are now using broad-band, low-frequency dipole arrays with state-of-the-art digital backends to search for extragalactic radio bursts at frequencies below $300\,\mathrm{MHz}$.

And yet, to date no FRBs have been detected below $300\,\mathrm{MHz}$ — despite both simultaneous, multi-frequency, targeted (Law et al. 2017; Sokolowski et al. 2018; Houben et al. 2019) and blind, wide-field (Coenen et al. 2014; Karastergiou et al. 2015; Tingay et al. 2015; Rowlinson et al. 2016; Sanidas et al. 2019) searches using the Low-Frequency Array (LOFAR), Murchison Wide-field Array (MWA) and Long-Wavelength Array (LWA).

Here we present LOFAR[3] high-band antenna (HBA; $110 - 188\,\mathrm{MHz}$), upgraded Giant Metre Wavelength Radio Telescope (uGMRT; $200 - 450\,\mathrm{MHz}$) and CHIME/FRB ($400 - 800\,\mathrm{MHz}$) observations of FRB 20180916B. These observations achieve, by far, the lowest-frequency FRB detections to date, and provide an unprecedented data set to investigate whether the observed activity of the source systematically depends on radio frequency. We present the observations in §2 and §3, and discuss their implications for FRB source and emission models in §4. We conclude in §5.

2. OBSERVATIONS

Figure 1 presents an overview of the LOFAR, uGMRT and CHIME/FRB observations taken in 15 different, and not necessarily contiguous, 16.3-day cycles of activity of FRB 20180916B (as determined from CHIME/FRB detections). Throughout this paper, a dispersion constant of $k_{\mathrm{DM}} = (2.41 \times 10^{-4})^{-1}\,\mathrm{MHz^2\,cm^3\,pc^{-1}\,s}$ is used, following the pulsar convention (Manchester & Taylor 1972; see discussion in Kulkarni 2020).

2.1. *LOFAR*

FRB 20180916B was observed with LOFAR (van Haarlem et al. 2013) using its beam-formed modes (Stappers et al. 2011) for 112 hours on 128 occasions between 2019 June 6 and 2020 August 26. The COBALT correlator and beamformer (Broekema et al. 2018) coherently combined signals from the HBA antennas of the LOFAR Core stations to create a tied-array beam pointing to the best-known position of FRB 20180916B. The best CHIME/FRB localization of $\alpha_{\mathrm{J2000}} = 01^{\mathrm{h}}57^{\mathrm{m}}43^{\mathrm{s}}$, $\delta_{\mathrm{J2000}} = +65°42'00''$ (estimated uncertainty of $\sim 2'$) was used until 2019 August, while the much more-

---

[3] Half of these LOFAR observations (56 hours out of a total 112 hours) are also reported on by an independent group in parallel (Pastor-Marazuela et al. 2020).
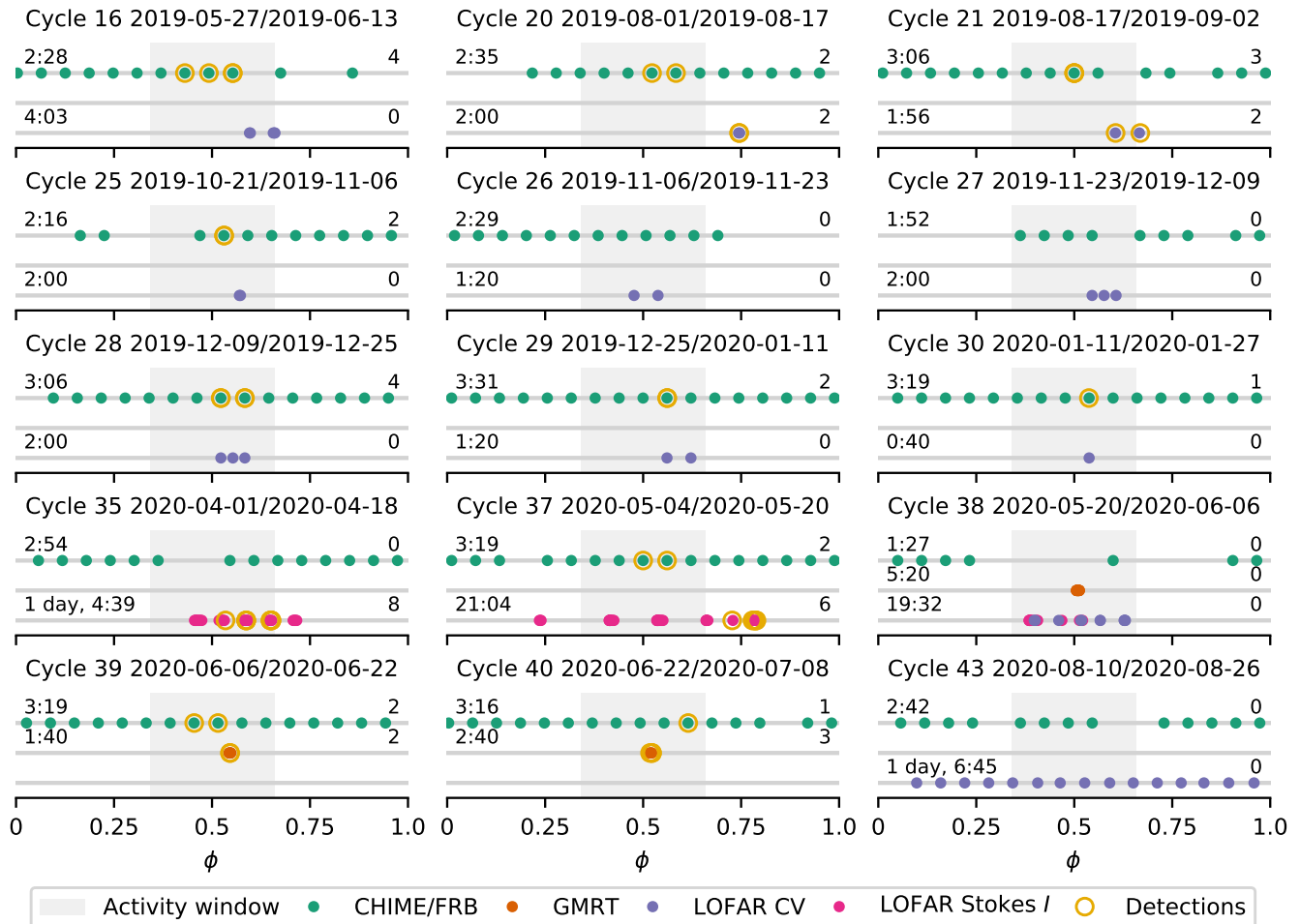
Figure 1. Summary of per-cycle observations for CHIME/FRB (top row), uGMRT (middle row) and LOFAR (bottom row), as a function of activity phase. In each row the text on the left shows the total observing time (in hours and minutes) and the text on the right shows the total number of bursts detected in the cycle, for the respective telescopes. Only cycles in which uGMRT and LOFAR were observing are shown. Note that the new CHIME/FRB detections reported here are in Cycle 32 and later and that not all of them are shown in this figure. Cycle 1 is the first cycle in which CHIME/FRB detected a burst from the source, with $\phi_0 = 58369.40$ MJD, such that $\phi = 0.5$ is the mean of the folded phases of the CHIME/FRB bursts. "CV" stands for complex voltage data.

precise position from the EVN localization, $\alpha_{\mathrm{J2000}} = 01^{\mathrm{h}}58^{\mathrm{m}}00.7502^{\mathrm{s}}$, $\delta_{\mathrm{J2000}} = +65°43'00.3152''$ (2.3-mas uncertainty), by Marcote et al. (2020) was used afterwards. As all observations used either the innermost 22 or 23 LOFAR Core stations, the $\sim 3'$ FWHM of the tied-array beam encompassed the actual celestial position of FRB 20180916B in the observations prior to 2019 August. Observations were obtained with the source at altitudes ranging from 37° up to culmination at 77°, with 86% of the observations being obtained at altitudes of 60° or higher.

The earliest LOFAR observations (up to approximately source activity cycle 26; see Figure 1) were scheduled in response to CHIME/FRB detections. After the identification of a 16.3-day activity period by

CHIME/FRB, observations were scheduled close to the peak in the CHIME/FRB-derived activity window (cycle 26 and later). The observations in cycle 43 were intended to broadly cover the full range of activity phases.

For all observations, 400 subbands of 195.3125 kHz each were recorded, covering observing frequencies of 110 to 188 MHz for a total bandwidth of 78.125 MHz. For 56 hours of the observations, the Cobalt correlator and beamformer generated total-intensity Stokes I filterbank data, with a frequency and time resolution of 3.05 kHz and 983.04 μs, respectively. Nyquist-sampled, dual-polarization complex voltages ("CV" data, with 195.3125 kHz frequency resolution and 5.12 μs time resolution) were recorded for the other 56 hours of observations. For FRB 20180916B's dispersion measure
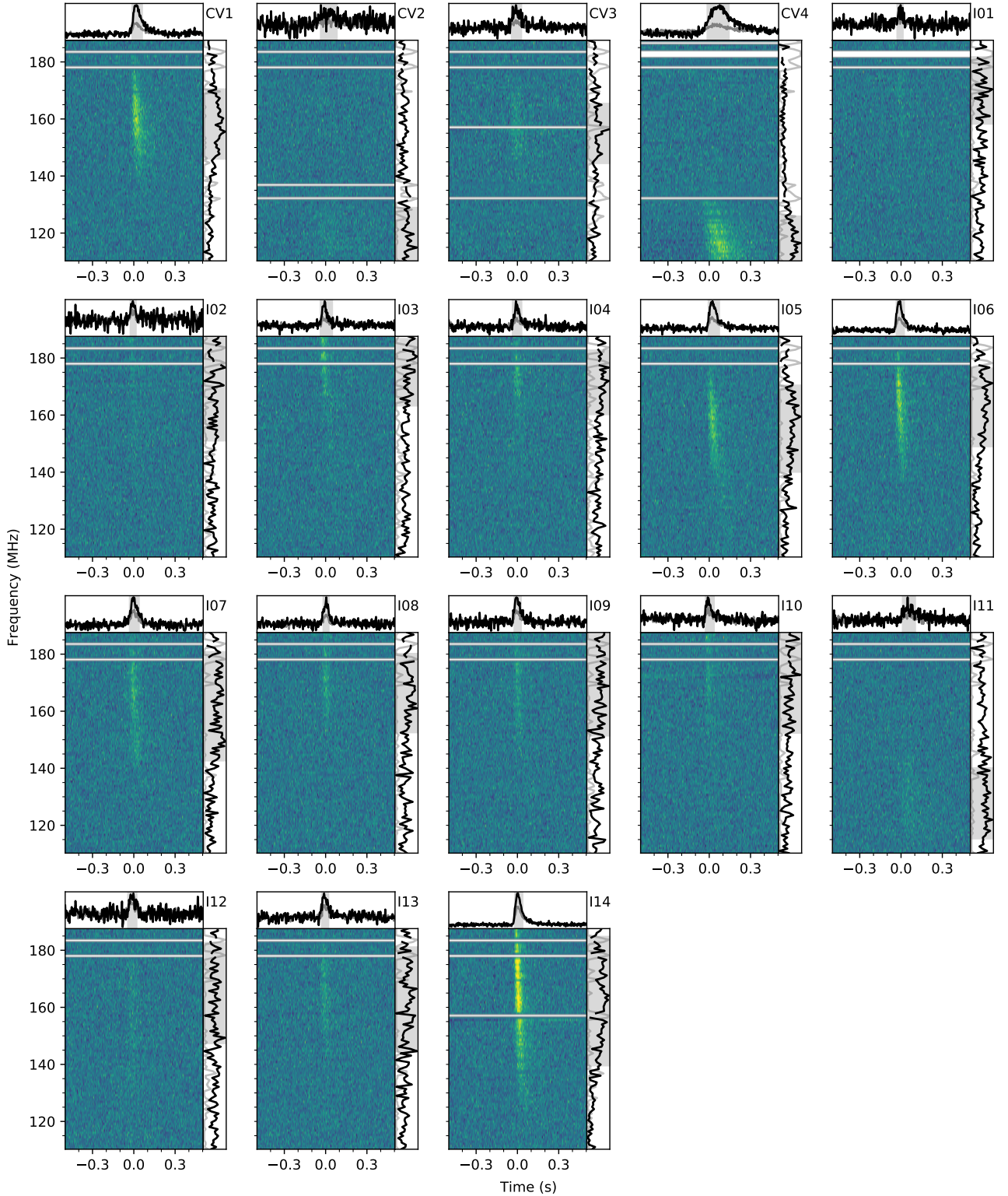
Figure 2. Dynamic spectra of bursts detected with LOFAR. All bursts are dedispersed to DM $= 348.772\,\mathrm{pc\,cm^{-3}}$, the best-fit DM from Nimmo et al. (2020). These dynamic spectra have been averaged to a time resolution of 3.93 ms and a frequency resolution of 0.781 MHz. The color scale is set to be the same in all panels. The horizontal white bars indicate parts of the spectra where radio frequency interference was masked. Time-averaged spectra are shown at the right-hand side of each panel (black), as well as the fraction of averaged frequency and time points that were masked to excise radio frequency interference (light grey). The grey band in this panels denotes the burst FWHM in frequency. The top panel shows the frequency-averaged pulse profile over the spectral envelope of the burst (black) and the entire band ($110 - 188$ MHz; gray), with the burst FWHM denoted by the grey band. Events labeled "CVn" are from complex voltage data, while those labeled "In" are from total intensity data.

DM = $348.772 \pm 0.006 \, \mathrm{pc\,cm^{-3}}$ (Nimmo et al. 2020) the dispersion delay from infinite frequency to the top of the observed LOFAR band (188 MHz) is 40.9 s, and the delay within the band, from 188 MHz down to 110 MHz, is 78.7 s.

The CV data allow for coherent dedispersion, a technique that we are employing to search for FRBs and millisecond pulsars using LOFAR and our DRAGNET GPU cluster (Bassa et al. 2017a,b). In this paper, we apply coherent dedispersion for burst characterization (see §3), but given the large burst widths, and to allow for a homogeneous burst search of both the Stokes I and the complex voltage datasets, we chose not to coherently dedisperse the CV data for the purposes of searching for signals. Instead, the complex voltage data were channelized, time averaged and the polarizations were squared and summed offline to form Stokes I filterbanks with the same time and frequency resolution as the Stokes I filterbanks (3.05 kHz and 983.04 µs) generated by COBALT in real time. To reduce their size, these filterbanks were first averaged in frequency by a factor 16 with `digifil` (van Straten & Bailes 2011), using incoherent dedispersion to DM = $350 \, \mathrm{pc\,cm^{-3}}$. With this setup, dispersive smearing due to incoherent dedispersion at the DM of FRB 20180916B varies from 1.3 to 6.7 ms over the LOFAR band. This temporal smearing is negligible compared to the burst widths. Radio frequency interference (RFI) was identified using the `rfifind` tool from the PRESTO software (Ransom 2001; Ransom et al. 2002) and replaced with random noise of the appropriate mean and standard deviation. Next, dedispersed time series were generated between DMs of 300 to $400 \, \mathrm{pc\,cm^{-3}}$, with steps of $0.1 \, \mathrm{pc\,cm^{-3}}$ using the GPU-accelerated DEDISP dedispersion library (Barsdell et al. 2012).

To maximize sensitivity towards possibly narrow-band radio bursts (motivated by Gourdji et al. 2019; Kumar et al. 2021), these time series were created for the full observing band (110–188 MHz), as well as three overlapping halves (110–149 MHz, 130–169 MHz and 149–188 MHz), and seven overlapping quarters of the band (110–129 MHz, 120–139 MHz, etc.). These time series were cross-correlated with top-hat functions with widths up to 150 ms, using a GPU-accelerated version of `single_pulse_search.py` from PRESTO to search for bursts. All candidate burst events with S/N > 7 were visually inspected to distinguish bursts from residual RFI. For the 12 data sets with known bursts, we verified that the burst selection is complete by also assessing the burst candidates using the FETCH deep-learning based classifier (Agarwal et al. 2020).

2.2. uGMRT

The uGMRT (Gupta et al. 2017) observations of FRB 20180916B were carried out on three different days: 2020 May 29, 2020 June 15 and 2020 July 1. The observations were intentionally scheduled close to the peak of the CHIME/FRB-derived activity window. On 2020 May 29, we used both Band 2 (180–280 MHz) and Band 3 (250–350 MHz) simultaneously with two phased-array beams employing two sub-arrays: one sub-array with ten central square antennas at Band 2 (180–280 MHz) out of the available 29 antennas, and another sub-array at Band 3 (250–500 MHz) using the remaining 19 antennas. We used the uGMRT Wideband Backend (GWB; Reddy et al. 2017) to record coherently dedispersed total-intensity filterbank data with the passband split into 2,048 channels with 327.68 µs sampling time in both phased-array beams. The observations were divided into eight 20-minute sessions with a provision to re-phase the sub-arrays in between the sessions to account for the temporal instrumental gain and ionospheric changes. We used the same setup on June 15 with five 20-minute sessions, but the Band 2 data were not usable due to strong RFI. On 2020 July 1, we observed only in Band 3 set to 250–450 MHz using 24 antennas in four 40-minute sessions. The coherently dedispersed filterbank data were recorded with 81.92-µs time resolution and 2,048 frequency channels across the 200-MHz band. On all three days we have also recorded "ON" source and "OFF" source data on 3C48 for calibration purposes.

To prepare the data for searching, we identified and mitigated narrow-band RFI and broad-band time-domain RFI using `gptool` (Susobhanan et al. 2020). The single-pulse search was carried out using a machine-learning technique based on Zhang et al. (2018). We have trained our convolutional neural network model using archival uGMRT data and simulated CHIME/FRB-like FRBs with various burst morphologies. The details of our implementation will be published elsewhere. This particular search is tuned for $200 \leq \mathrm{DM} \leq 500 \, \mathrm{pc\,cm^{-3}}$ and is sensitive to pulse widths up to 256 ms. The dynamic spectra of candidates were visually examined to distinguish astrophysical signals from spurious RFI.

2.3. CHIME/FRB

CHIME/FRB searches intensity data from 1,024 stationary synthesized beams for dispersed transients over a ∼200 deg² field-of-view in the 400–800 MHz octave in real time (CHIME/FRB Collaboration 2018). The intensity data have a 0.98304-ms time resolution and 16,384 frequency channels.

The median daily exposure of the experiment to the sky position of FRB 20180916B is 746 s (i.e., the time spent by the source within the FWHM of the synthesized beams at 600 MHz). The transit time of the source through the primary beam of the instrument, however, is much longer ($\sim$40 minutes), albeit with significant variation in sensitivity that is still in the process of being quantified outside of the FWHM of the synthesized beams.

3. RESULTS

All bursts presented here have been dedispersed to DM = 348.772 pc cm^{-3}, as determined from aligning sub-structure in EVN voltage data at 1 μs resolution (Nimmo et al. 2020). We decided against optimizing individual burst DMs, as DM and burst morphology are known to be covariant (especially for the majority of low S/N 'smudgy' bursts; Gourdji et al. 2019) and there is as-of-yet no evidence for DM evolution of FRB 20180916B (PR3).

3.1. LOFAR

A total of 18 bursts were detected using LOFAR: 14 were found in the full-bandwidth data, and another 4 fainter bursts were identified in the time series generated from the half- and quarter-bandwidth data segments. The dynamic spectra of these bursts are presented in Figure 2. Four of the bursts occurred during complex voltage observations, and thus have available polarimetric information. These are labelled CV1 through CV4, while the bursts obtained in total-intensity Stokes I data are labelled I01 through I14.

The LOFAR burst properties were determined by fitting Gaussian profiles to the time and frequency averages of the dynamic spectra to obtain their arrival times, temporal and spectral widths (FHWM) and emission frequencies (Table 1). All observed bursts are band-limited, with spectral widths (defined as FWHM) ranging from 20 to 50 MHz, and the majority of the bursts, 15 out of 18, peaking in brightness above 160 MHz. The temporal width of the bursts varies between 40 ms for bursts peaking in the top of the LOFAR band ($\sim$ 180 MHz) to 160 ms near the bottom of the LOFAR band ($\sim$ 120 MHz).

To calibrate the LOFAR detections we have subtracted the mean of an off-burst region in each frequency channel and divided by the standard deviation of the off-burst region. We then convert each channel i from S/N to flux units using the radiometer equation:

$$\Delta S_i = \frac{T_{\mathrm{sys},i}}{G_i \sqrt{n_{\mathrm{p}} \Delta \nu_i t_{\mathrm{s}}}}, \qquad (1)$$

where $T_{\mathrm{sys},i}$ is the system temperature (receiver and sky), G_i the gain, $n_{\mathrm{p}} = 2$ the number of summed polarizations, $\Delta \nu_i$ the channel bandwidth and t_{s} the sampling time. For the calculation of T_{sys} and G we take into account the number of Core stations used and we correct for the zenith-angle dependence as described by Kondratiev et al. (2016). We calculate these values at the times of the burst detections. In the center of the band ($\sim$149 MHz) $T_{\mathrm{sys}} \approx 1,090$ K (note that FRB 20180916B is at a Galactic latitude of $b = 3.7°$) and $G \approx 4.4$ K Jy^{-1}, on average. We repeat this measurement using six different independent, but adjacent, $\sim$ 100-ms off-pulse regions in the same observation as the burst and quote the average (band-averaged) fluence and peak flux of the bursts as well as the standard deviation across the six samples in Table 1. Note that the systematic uncertainty in the flux measurements could be larger than reported in the Table, due to unaccounted for contributions from the ionosphere and the Galactic plane or other bright sources in the primary beam of the HBAs.

Even after dedispersion to the best-fit DM from Nimmo et al. (2020), the brightest LOFAR bursts show residual time delays towards lower observing frequencies, with one burst (CV4) broadening with decreasing frequency. Due to the absence of visible burst sub-structure, it is unclear if these effects are due to DM underestimation, multi-path scattering, or the frequency drifts of unresolved sub-bursts (i.e. the 'sad trombone' effect Hessels et al. 2019). Deviations from the canonical $\Delta t \propto \nu^{-2}$ dispersion relation are expected at low radio frequencies (see Hassall et al. 2012, and references therein), and it is also possible that the residual time delays in CV4 result from such deviations.

To measure a scattering timescale, we use a least-squares fitting routine, previously developed for CHIME/FRB bursts (e.g., Josephy et al. 2019; CHIME/FRB Collaboration et al. 2019a), to model the dynamic spectra of the LOFAR bursts. We analyze the three brightest bursts that can be coherently dedispersed: bursts CV1, CV3 and CV4, where dspsr (van Straten & Bailes 2011) was used to generate coherently dedispersed single pulse profiles. We keep the DM fixed at DM = 348.772 pc cm^{-3} (Nimmo et al. 2020) and assume the bursts consist of only one component. We reference the scattering timescale to 150 MHz and keep the scattering index fixed to -4. The results are provided in Table 2 and Figure 3. The measured scattering timescale for the two bursts with highest S/N (CV1 and CV4) is $\sim$50 ms at 150 MHz. The other measured timescale, for burst CV3, is more uncertain due to the low detection S/N and narrow bandwidth of the burst.

Table 1. Burst parameters. See §3 for a description of how parameters were determined. For all bursts, arrival times and burst width σ_t are computed for DM = 348.772 pc cm^{-3} (Nimmo et al. 2020).

Burst	Barycentric arrival time at $\nu = \infty$ (UTC)	(MJD)	ϕ	σ_t[a] (ms)	ν_low (MHz)	ν_high (MHz)	S/N[b]	Fluence (Jy ms)	Peak flux density (Jy)
				LOFAR					
CV1	2019-08-13T03:55:04.386	58708.16417	0.74490	73(3)	133.7	182.8	28.6	148(8)	4.7(1)
CV2[c]	2019-08-13T04:04:24.099	58708.17064	0.74529	119(35)	109.8	139.0	3.9	26(9)	1.52(9)
CV3	2019-08-27T05:13:41.727	58722.21786	0.60550	72(7)	133.9	175.9	11.4	50(12)	2.20(8)
CV4	2019-08-28T05:56:10.932	58723.24730	0.66854	158(7)	109.8	135.6	25.5	210(24)	3.8(2)
I01[c]	2020-04-10T16:10:15.975	58949.67733	0.53444	43(10)	146.5	188.0	5.1	28(10)	2.11(8)
I02[c]	2020-04-11T12:59:33.109	58950.54492	0.58756	42(8)	131.3	188.0	6.3	36(9)	1.74(9)
I03	2020-04-11T13:34:29.179	58950.56918	0.58905	87(8)	151.5	188.0	11.8	82(10)	2.9(2)
I04	2020-04-11T14:31:53.260	58950.60904	0.59149	66(6)	148.9	188.0	13.2	66(11)	2.66(8)
I05	2020-04-12T13:00:37.497	58951.54570	0.64885	80(4)	124.8	185.7	21.5	131(9)	3.52(7)
I06	2020-04-12T13:47:53.211	58951.57852	0.65086	58(2)	135.2	188.0	27.8	138(12)	5.1(1)
I07	2020-04-12T14:03:49.545	58951.58959	0.65154	69(4)	123.5	188.0	20.0	97(8)	3.7(1)
I08	2020-04-12T14:22:53.501	58951.60283	0.65235	41(4)	138.6	188.0	11.5	62(9)	2.77(9)
I09	2020-05-16T11:35:19.481	58985.48715	0.72732	50(5)	128.2	188.0	12.7	90(36)	3.2(6)
I10	2020-05-17T08:03:36.316	58986.34012	0.77955	63(7)	134.7	188.0	10.5	54(9)	2.5(1)
I11[c]	2020-05-17T09:06:12.516	58986.38360	0.78222	93(14)	109.8	152.5	7.5	39(7)	1.50(5)
I12	2020-05-17T11:12:52.169	58986.47156	0.78760	65(8)	129.7	188.0	10.0	50(8)	2.2(1)
I13	2020-05-17T11:23:34.096	58986.47899	0.78806	51(5)	126.1	188.0	12.8	62(7)	3.44(4)
I14	2020-05-17T12:58:52.223	58986.54517	0.79211	57(2)	116.9	188.0	38.5	313(10)	10.72(7)
				uGMRT					
G1	2020-06-15T04:25:47.176	59015.18457	0.54590	17(3)	270[d]	350[d]	25.0	161(71)	8(2)
G2	2020-06-15T04:32:28.540	59015.18922	0.54619	12(4)	280[d]	350[d]	8.5	26(11)	2.3(4)
G3	2020-07-01T01:16:03.761	59031.05282	0.51763	39(7)	325[d]	410[d]	6.1	33(14)	1.6(3)
G4	2020-07-01T03:03:41.718	59031.12757	0.52220	18(3)	375[d]	450[d]	12.0	27(11)	2.5(4)
G5	2020-07-01T03:17:40.549	59031.13727	0.52280	98(8)	300[d]	450[d]	16.4	178(58)	3.3(8)
				CHIME/FRB					
CF39	2020-02-19T23:54:17.856	58898.99604	0.43087	4.8(6)	418	520	8.8	>1.8(4)	>0.4(2)
CF40	2020-02-20T00:10:50.592	58899.00753	0.43158	5.5(7)	429	526	11.8	>1.9(6)	>0.3(2)
CF41	2020-02-21T00:10:23.808	58900.00722	0.49279	2.6(2), 2.7(2)	417	469	24.7	>5(2)	>0.7(3)
CF42	2020-03-24T21:33:36.576	58932.89834	0.50694	3.1(3)	403	460	13.0	>1.6(6)	>0.4(2)
CF43	2020-04-23T19:35:03.264	58962.81601	0.33901	0.54(3)	400	693	12.6	>0.9(5)	>1.5(6)
CF44	2020-04-24T19:49:22.944	58963.82596	0.40085	1.0(1)	545	674	9.2	>2.0(5)	>0.8(3)
CF45	2020-05-12T18:33:52.128	58981.77352	0.49991	0.7(2), 2.9(1)	690	800	22.7	12(3)	1.7(6)
CF46	2020-05-13T18:26:35.808	58982.76847	0.56084	3.7(4)	403	469	12.2	2.2(7)	0.4(3)
CF47	2020-06-13T16:33:47.232	59013.69013	0.45439	2.7(2)	400	479	19.3	>4(1)	>0.9(4)
CF48	2020-06-14T16:22:57.504	59014.68261	0.51516	0.72(3), 2.6(4)	539	639	15.4	14(4)	3.0(8)
CF49	2020-07-02T15:22:45.120	59032.64080	0.61487	4.2(2)	407	462	16.2	>5(1)	>0.6(3)
CF50	2020-07-17T13:55:55.200	59047.58050	0.52973	3.7(2)	400	432	17.7	>4(1)	>0.6(2)
CF51	2020-07-17T14:04:18.048	59047.58632	0.53009	2.5(2)	443	511	11.5	>0.8(2)	>0.2(2)
CF52	2020-08-01T13:26:53.376	59062.56034	0.44705	2.7(4)	428	462	8.3	>0.9(3)	>0.3(2)
CF53	2020-09-03T11:12:54.720	59095.46730	0.46217	2.9(3)	536	688	11.1	5(1)	1.1(4)
CF54	2020-09-04T10:54:30.528	59096.45452	0.52263	1.19(9)	707	800	15.8	>2.5(6)	>1.2(4)
CF55	2020-09-19T09:48:59.328	59111.40902	0.43840	6.4(7)	400	447	10.9	>1.8(3)	>0.3(2)

[a] Burst width (FWHM), for a Gaussian function fitted to the time series.

[b] Band-averaged S/N. Four LOFAR-detected bursts were found in a search of the half- and quarter-bandwidth data segments.

[c] Only detected in a sub-band search.

[d] Estimated by eye because baseline variations due to residual broad-band RFI prohibited fitting a model to the burst spectra.
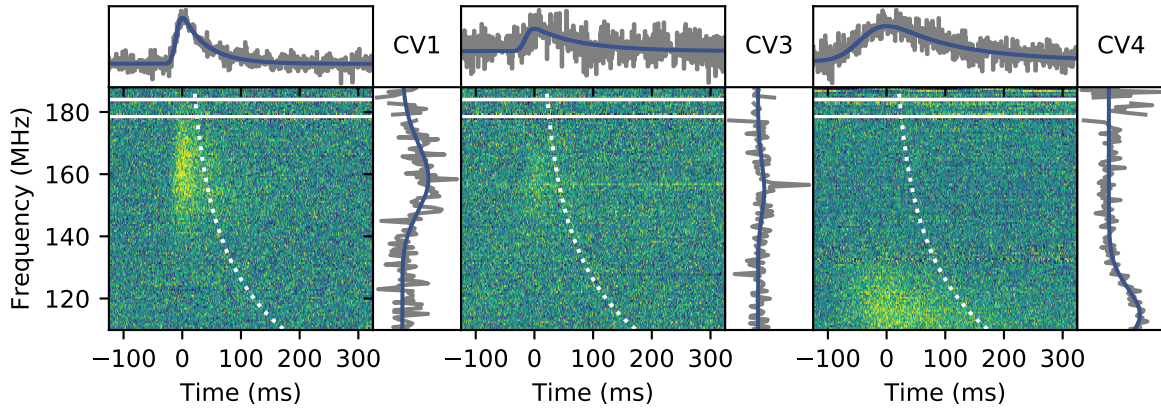
Figure 3. Least-squares burst model fits to LOFAR bursts CV1, CV3 and CV4, after coherent dedispersion. The model (solid blue line; Table 2) is overlayed on the band-averaged time series (top panel) and the time-averaged spectra (right panel). A fiducial scattering timescale of 50 ms (referenced at 150 MHz) is plotted on top of the dynamic spectra (white dotted line). The horizontal white bars indicate parts of the spectra where radio frequency interference was masked.

Table 2. Best-fit intrinsic width, scattering timescale (τ_s; at 150 MHz) and rotation measure (RM) for three of the LOFAR bursts. Only formal fit uncertainties are quoted; this is particularly relevant for the τ_s measurement of CV3 (see main text). The RMs are the observed values; they are not corrected for Doppler redshift or ionospheric contribution, although they are corrected for the Earth's motion. The corresponding ionospheric contribution, RM_{iono}, is reported, as calculated with `ionFR` (see main text).

Burst	Width	τ_s	RM_{obs}	RM_{iono}
	(ms)	(ms)	(rad m^{-2})	(rad m^{-2})
CV1	6.608(1)	54.142(4)	$-115.70(3)$	0.30(8)
CV3	8.313(4)	94.55(2)	$-114.45(9)$	0.34(4)
CV4	31.426(3)	46.692(3)	$-114.40(4)$	0.39(5)

3.2. Polarization analysis

We recorded polarization, using LOFAR's orthogonal linear feeds, for bursts CV1–4; three of these bursts are bright enough to perform polarimetric analyses. No additional polarization calibration, beyond that already implemented to form the individual station and Core tied-array beams, was performed and, thus, slight degradation in the polarization fraction could arise, e.g., from the thermal expansion of the cables. The absence of an absolute polarization calibration also prevents us to compare the polarization angle (PA) across different bursts. The frequency resolution has been increased to ~ 12 kHz (16 channels synthesized within each 195-kHz subband) to have an intra-channel depolarization smaller than 1% across the whole band at the value of rotation measure (RM) reported by CHIME/FRB Collaboration et al. (2019a). We measured the RM value of each burst by using RM synthesis[4] (Burn 1966; Brentjens & de Bruyn 2005) and a deconvolution algorithm (Heald 2009); the Stokes parameters of each burst have been corrected for the resulting value.

We report the polarization profiles for the three bursts in Figure 4, using the coherently dedispersed pulse profiles from §3.1. The linear polarization fractions of CV1, CV3 and CV4 are roughly 70%, 60% and 30%, respectively — much lower than the $\sim 100\%$ reported at higher frequencies of $300-1700$ MHz (CHIME/FRB Collaboration et al. 2019a; Chawla et al. 2020; Nimmo et al. 2020). Noutsos et al. (2015) performed a long observation of PSR B2217+47 to study the depolarization fraction as a function of the hour angle (HA) for LOFAR. They found a depolarization fraction $< 10\%$ for $|HA| < 6$ hours and zenith angle $< 50°$. Our observations of FRB 20180916B are well within this range, with a maximum hour angle

of 2.1 hours and a maximum zenith angle of 20.3°. Given also the absence of any visible artifacts in the Faraday dispersion function that could indicate the presence of signal leakage, such as a peak at $RM = 0$ rad m^{-2} or symmetric peaks around $RM = 0$ rad m^{-2}, we conclude that the observed depolarization towards lower radio frequencies is predominantly astrophysical in origin.

Part of the depolarization at lower frequencies could therefore be intrinsic to the source emission or be related to extrinsic propagation effects. In particular, CV4 is observed at the lowest frequencies and has the lowest linear polarization fraction, which is compatible with depolarization due to scattering, as observed in some pulsars (e.g. Noutsos et al. 2015; Xue et al. 2019). As at higher frequencies, the circular polarization fraction here is consistent with 0%. The PA curve is nearly flat at higher frequencies, though subtle variations are seen on short timescales (Nimmo et al. 2020). While the PA curve of CV4 is consistent with being flat ($\chi^2_{red} = 0.8$), the PA curve of the brightest burst, CV1, shows a hint of a decrease at later times, with a $\chi^2_{red} = 2.4$ with respect to a straight line.

The lack of refined polarization calibration is not expected to affect the RM values measured by LOFAR (e.g., Sobey et al. 2019), which are reported in Table 2. We compare the new LOFAR RM values obtained here with other measurements presented by CHIME/FRB Collaboration et al. (2019a) and Chawla et al. (2020). The ionospheric contribution to the observed burst RMs was determined using `ionFR`[5] (Sotomayor-Beltran et al. 2013), which utilizes data from the International Geomagnetic Reference Field and IONosphere map EXchange (IONEX) global ionospheric maps. The resulting values are shown in Figure 5 as a function of date and source activity phase, as measured by PR3 and refined in §3.5. There is a hint of RM values changing systematically as a function of activity phase, as measured by different instruments in different activity cycles. However, this trend could be spurious due to the low number of bursts, and more RM detections are needed to investigate this further.

3.3. uGMRT

We detected five bursts in the uGMRT data. Two in the 250–350-MHz band on 2020 June 15 and three in the 250–450-MHz band on 2020 July 1. We did not detect any bursts on 2020 May 29. The burst dynamic spectra are presented in Figure 6. To calibrate the bursts we have used the counts per Jansky estimated for every clean frequency channel from the "ON" and "OFF" data

---

[4] https://github.com/CIRADA-Tools/RM-Tools
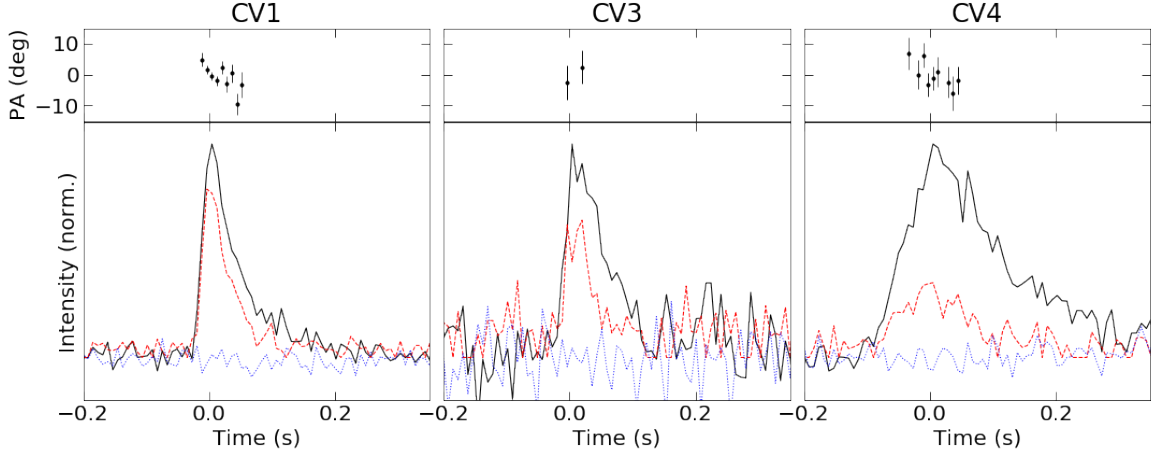
[5] https://github.com/csobey/ionFR

Figure 4. Polarization profiles obtained for the three LOFAR bursts with available CV data and sufficient S/N. The black curve is the total intensity, the red dashed curve is the linear polarization, after correcting for Faraday rotation, and the blue dotted curve is the circular polarization. For clarity, the profiles have been normalized to all have unitary peak intensities, and are plotted with a time resolution of 7.8125 ms. The PA curves are reported in the top panel of each profile and are rotated by an arbitrary angle in order to be centered around zero.
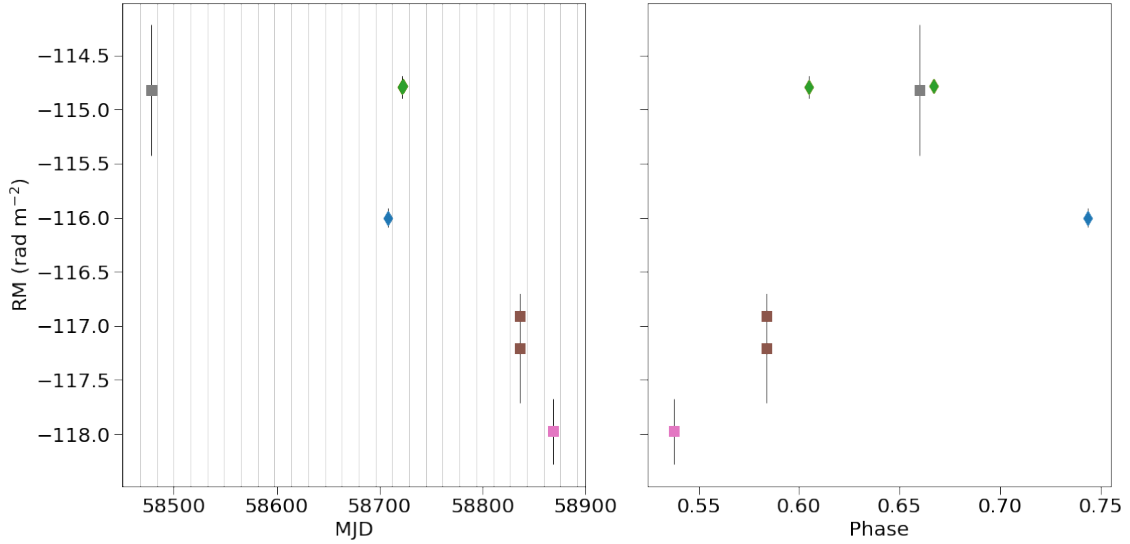
Figure 5. Measured RMs for FRB 20180916B from this work (diamond symbols), CHIME/FRB Collaboration et al. (2019a) and Chawla et al. (2020) (square symbols). The RMs are corrected for the ionospheric contribution and plotted with 1-σ error bars. Left: Plot as a function of time (in MJD), where vertical lines represent phase zero of the different activity cycles of the source. Right: Plot as a function of the source activity phase. The different colors of the data points represent different source cycles.

from 3C48. The conversion factors are multiplied with the filterbank counts to get the calibrated data. The measured peak flux densities and fluences are presented in Table 1.

We caution the reader not to over-interpret the spectral structure of the uGMRT bursts, due to the baseline variations from residual broad-band RFI in the dynamic spectra. The four sub-bursts in burst G5, however, are real. Using DM_phase[6] (Seymour et al. 2019) we align the sub-bursts of G5 and find an optimum DM = 349.5±0.1 pc cm^{-3}. In Figure 7 we show a comparison of the dynamic spectra of the bursts, dedispersed to the fiducial and optimum DM values.

---

[6] https://github.com/danielemichilli/DM_phase
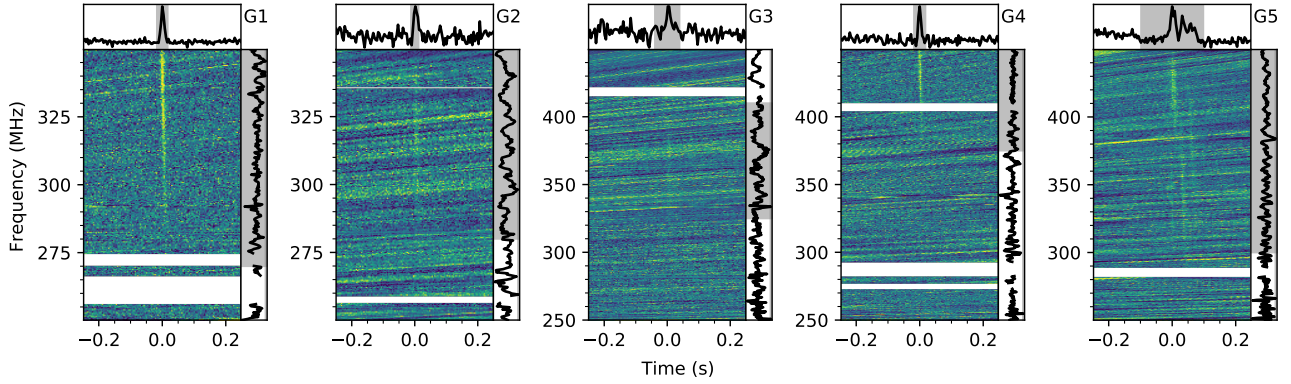
Figure 6. Dynamic spectra of bursts detected with the uGMRT. These dynamic spectra have been averaged to a time resolution of 3.93 ms and a frequency resolution of 0.391 MHz. Note the different receiver bandwidth for bursts G1–2 and G3–5. Otherwise, the plot features are the same as in Figure 2. The diagonal striations in the bandpass are due to residual broad-band RFI.
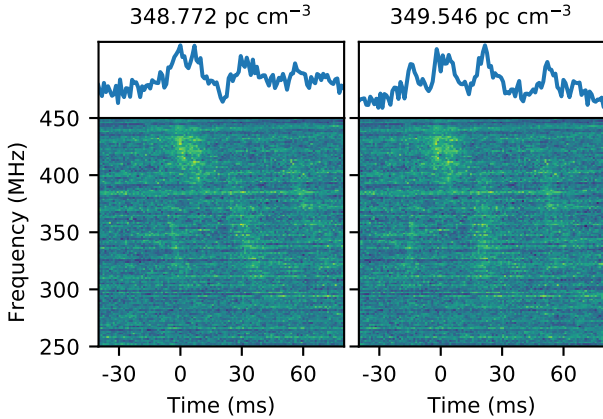
Figure 7. Burst G5 dedispersed to the best-fit DM from Nimmo et al. (2020) (left) and the optimum DM from aligning the sub-bursts (right; see main text).

3.4. *CHIME/FRB*

We present 17 new bursts detected by CHIME/FRB since PR3[7]. The burst dynamic spectra are presented in Figure 8. The morphologies of the bursts are comparable to those previously detected by CHIME/FRB; they exhibit narrow (50–150 MHz) bandwidths and sometimes show downward-drifting sub-bursts (CHIME/FRB Collaboration et al. 2019a).

We construct burst models and measure peak fluxes and fluences as in CHIME/FRB Collaboration et al. (2020a). In summary, we fit single- or multi-component models of dynamic spectra to the 0.98304-ms total-intensity data for each burst using a least-squares algorithm. Data are flux calibrated using transits of steady sources and scaled by the beam response using the best

---

[7] Note that the burst arrival times were previously announced at https://www.chime-frb.ca/repeaters/180916.J0158+65.

known location of FRB 20180916B and a model for the synthesized beams. For bursts detected outside of the FWHM of the synthesized beams at 600 MHz, peak fluxes and fluences are lower limits.

3.5. *Frequency dependence of periodic activity*

We recalculate the activity period and burst rate of FRB 20180916B using the same methods as described in PR3. We measure the activity period to be 16.33 ± 0.12 days, with a 5.2-day window, based on the now reported 55 CHIME/FRB detections. We use reference MJD $\phi_0 = 58369.40$ to put the average arrival time of the CHIME/FRB bursts at $\phi = 0.5$. We estimate the CHIME/FRB detection rate to be 0.8 ± 0.3 bursts per hour above a fluence threshold of 5.1 Jy ms for a ± 2.6-day interval around each cycle of activity (31 detections in 39.1 hours of exposure). In the 1σ activity window of ± 0.96 days around each cycle of activity, we estimate the detection rate to be $1.5^{+0.8}_{-0.6}$ bursts per hour (22 detections in 14.9 hours of exposure).

Both LOFAR and uGMRT predominantly observed FRB 20180916B during the 5.4-day activity window from PR3, though in later activity cycles LOFAR also targeted activity phases outside of the activity window (see Figure 1). Figure 9 shows the barycentred arrival times of the CHIME/FRB, uGMRT and LOFAR bursts folded on the activity period of 16.33 days — as a function of observing frequency, MJD, as well as cumulative fractions and histograms of the exposure of each instrument. The bursts observed with LOFAR fall between activity phases of $0.53 < \phi < 0.79$, corresponding to a range of 4.1 days within the 16.33-day activity period. This observed LOFAR activity window is nominally shorter than the 5.2-day activity window width observed from the CHIME/FRB bursts, but additional LOFAR observations may show the activity window to be wider. The average activity phase of the LOFAR
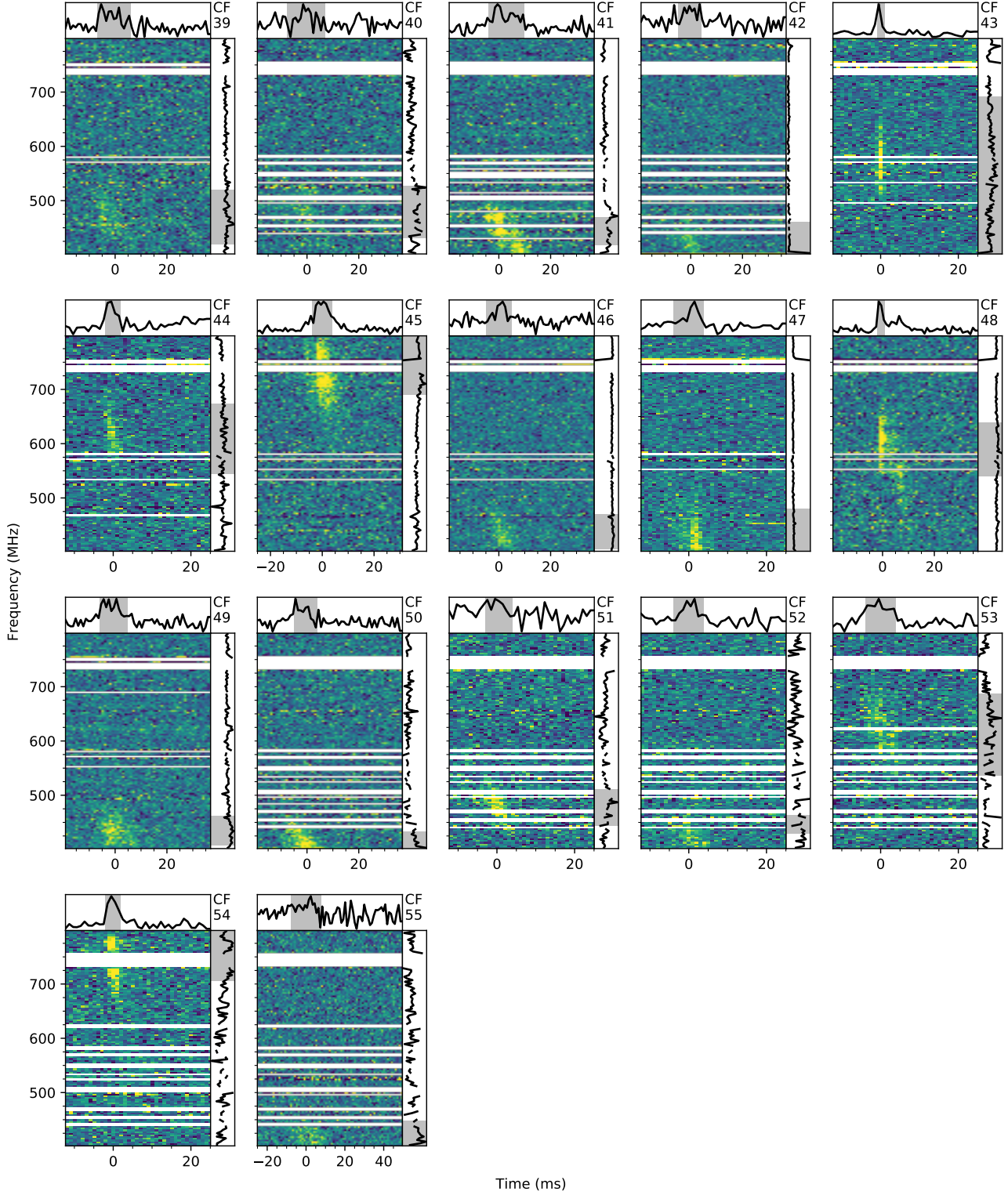
Figure 8. Dynamic spectra of bursts detected with CHIME/FRB. These dynamic spectra have time resolution of 0.98304 ms and have been averaged to a frequency resolution of 3.125 MHz. Otherwise, the plot features are the same as in Figure 2.
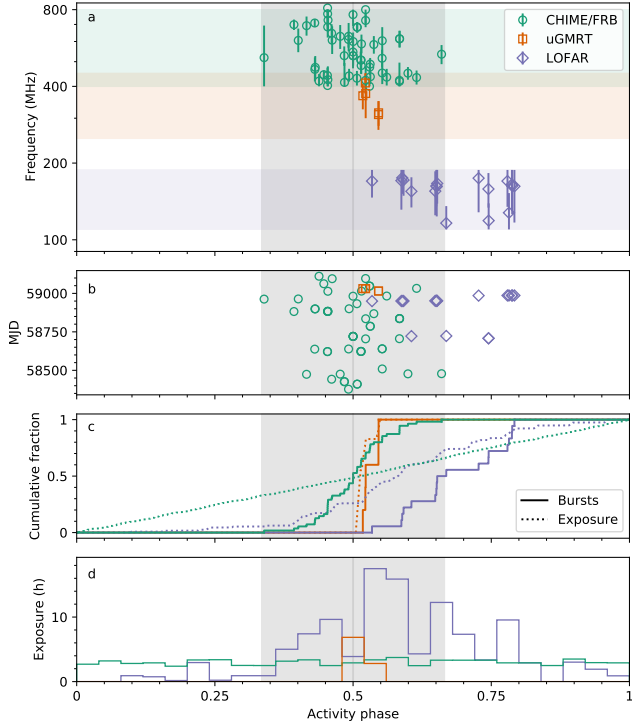
Figure 9. The activity phases of CHIME/FRB (blue circles), uGMRT (orange squares) and LOFAR (green diamonds) bursts folded on the 16.33-day activity period of FRB 20180916B. Panel (a) shows the activity phase of the bursts versus observing frequency. For each burst the spectral width is indicated by the error bars. Panel (b) shows the burst MJDs versus activity phase. The cumulative fraction of the number of bursts and the exposure are shown against activity phase in Panel (c), while Panel (d) displays the exposure as a histogram. The color coding is identical in the three panels. Whereas the CHIME/FRB exposure is almost uniform with activity phase, the exposure of the LOFAR observations is focused predominantly on the CHIME/FRB activity window. As the number of uGMRT observations is limited, the phase of the bursts is dominated by the phase of the observations.

bursts is $\phi \sim 0.66$, which is offset by 2.6 days from the average activity phase of FRB 20180916B determined from CHIME/FRB bursts (PR3). We note that the LOFAR burst detections as a function of activity phase are not just simply a reflection of the observing exposure. Through a two-sample Kolmogorov-Smirnov test we can reject the null hypothesis that the cumulative distribution functions of the LOFAR exposure and the LOFAR bursts shown in Figure 9 are drawn from the same distribution ($p \sim 10^{-10}$).

We performed numerical simulations to investigate the impact of the non-uniform exposure of the LOFAR observations as a function of activity phase (see Figure 9c and d) on the properties of the activity window at LO-
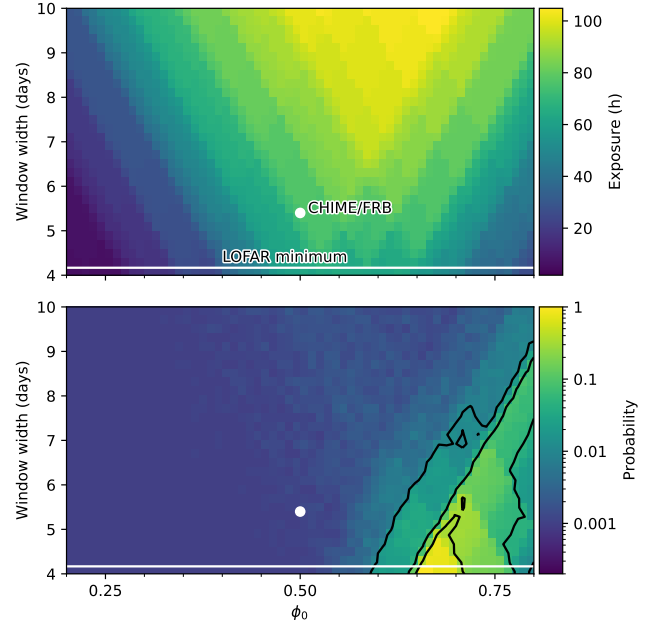
Figure 10. Constraints on the width w and central phase ϕ_0 of the LOFAR activity window. The top panel shows the exposure covered by the LOFAR observations as a function of the activity window properties. The dot indicates the CHIME/FRB activity window properties, while the horizontal line denotes the minimum LOFAR activity window width set by the observed bursts. The bottom panel shows the constraints on the width and central phase of the LOFAR activity window, based on numerical simulations where burst times of arrival are drawn from a uniform distribution within the activity window and 18 bursts are coincident with the LOFAR observations and the observed activity phases ($0.53 < \phi < 0.79$). The contours provide the 68%, 95% and 99% confidence regions.

FAR frequencies. We define an activity window by its width w and central phase ϕ_0, and compute the effective exposure of the LOFAR observations that fall within this activity window. The top panel of Figure 10 shows the LOFAR exposure given the properties of the activity window. As 18 bursts were observed with LOFAR, the exposure will provide the burst rate r as a function of w and ϕ_0. Given the activity window properties and the burst rate, we draw burst arrival times from a uniform distribution within the activity window for the activity cycles spanning the LOFAR observations (see Figure 1). For each w and ϕ_0 combination, we run mulitple simulations to obtain the fraction of simulations where the simulated bursts fall within both the LOFAR observations as well as the observed phase range of LOFAR bursts ($0.53 < \phi < 0.79$). The bottom panel of Figure 10 shows this fraction, which we treat as the probability that all simulated bursts fall within the observed LOFAR activity phase range.

The simulations show that the observed activity window of the LOFAR bursts is delayed with respect to the activity window observed by CHIME/FRB. The best fit parameters for w and ϕ_0 are determined through a Markov-Chain Monte Carlo analysis using the `emcee` software (Foreman-Mackey et al. 2013) to sample and maximize the probability that all simulated bursts coincident with the LOFAR observations fall within the observed LOFAR activity range. Flat priors were used for both parameters, though the width was limited to the observed minimum range of $w > 4.1$ days. The posterior distributions were obtained using 32 walkers for 20000 steps, well beyond 100 times the largest autocorrelation of the fitted parameters. After discarding a burn-in phase of 1000 steps, and thinning by 35 steps, we obtained $\phi_0 = 0.72^{+0.07}_{-0.04}$ and $w = 5.0^{+2.3}_{-0.8}$ d. These values correspond to a LOFAR burst rate of $r = 0.32^{+0.08}_{-0.04}$ hour^{-1} for a fluence limit of 26 Jy ms.

4. DISCUSSION

Our detection of 18 bursts from FRB 20180916B, using the LOFAR HBAs ($110 - 188$ MHz), constitutes the lowest-frequency FRB detections to date, by far, and provides a significant sample to compare with the arrival times and spectro-temporal/polarimetric properties of bursts detected at higher radio frequencies — including the five bursts from uGMRT ($200 - 450$ MHz) and 17 bursts from CHIME/FRB ($400 - 800$ MHz) that we present here for the first time.

4.1. *Lowest-frequency emission*

FRB 20180916B already held the record for the FRB with the lowest-frequency emission detected to date. Using the GBT and SRT, respectively, Chawla et al. (2020) and Pilia et al. (2020) previously presented a total of 10 burst detections at frequencies as low as 300 MHz. Here we present 18 bursts detected in the 110–188-MHz band. Notably, the majority of these bursts are brighter in the top-half of the band, but burst CV4 clearly demonstrates that emission can be detected down to at least 110 MHz (Figure 2). Searches for FRB 20180916B emission at radio frequencies < 100 MHz are thus well motivated, and are underway using joint observations with LOFAR and NenuFAR (New Extension in Nançay Upgrading LOFAR; Bondonneau et al. 2020). These observations can better quantify whether the observed burst rate is systematically reduced at lower radio frequencies. While only three of the 18 bursts we have observed here are emitting predominantly in the lowest part of the LOFAR HBA band ($110 - 140$ MHz), one must take observational biases like increased sky temperature ($T_{\rm sky}$) and larger pulse width into account (our detection metric scales as $F/\sqrt{w}$, where F and w are burst fluence and

width, respectively). The current sample is too small to make robust statements about the burst rate declining towards the bottom of the LOFAR HBA band.

Similarly, the detection of FRB 20180916B at $110 - 188$ MHz provides renewed hope for detections in wide-field, low-frequency surveys (e.g., Sanidas et al. 2019).

The simple fact that FRB 20180916B is visible at 110 MHz sets new requirements on the emission mechanism and constraints on the effect of free-free absorption in the local medium. Based on the lack of free-free absorption at 300 MHz, Chawla et al. (2020) argued that FRB 20180916B is not associated with a hyper-compact HII region or a young (< 50 yr) supernova remnant. This is consistent with the lack of local Hα emission or a persistent radio counterpart, as shown by Tendulkar et al. (2020) and Marcote et al. (2020), respectively. Here we show that the circumburst environment is optically thin to free-free absorption at 110 MHz. Considering an ionized nebula of size $L_{\rm pc}$, and DM < 70 pc cm^{-3} (Marcote et al. 2020). We use the following expression for the optical depth due to free-free absorption (Condon & Ransom 2016):

$$\tau_{\rm ff} = 1.6 \times 10^{-3} \times \left(\frac{\rm T}{10^4 \rm K}\right)^{-1.35} \times \left(\frac{\nu}{1 \rm GHz}\right)^{-2.1} \\ \times \frac{1}{\rm f_{eff} L_{pc}} \times \left(\frac{\rm DM}{70 \rm\ pc\ cm^{-3}}\right)^2 \ll 1, \quad (2)$$

where $\rm f_{eff}$ accounts for the volume-filling factor and the electron density fluctuation in the circum-burst medium. For $\rm f_{eff} = 1$, we find L $\gg 0.16$ pc $(\rm T/10^4$ K$)^{-1.35}$. The Crab nebula, for comparison, is about 1.7 pc in radius. Piro (2016) discusses how a surrounding supernova remnant can absorb bursts at low radio frequencies. In the context of that work, our detection of a burst down to 110 MHz implies a source age of at least $100 - 600$ yrs, for assumed ejecta masses between $3 - 10\,M_\odot$. Similarly, Marcote et al. (2020) discuss how the relatively low RM and lack of a persistent radio counterpart constrain the age of FRB 20180916B to be ≥ 300 yrs, in the context of models that describe it as a young flaring magnetar in a dense nebula (Metzger et al. 2019).

Models that describe FRBs via synchrotron maser emission from decelerating relativistic blast waves predict that the intrinsic FRB fluence is lower at lower radio frequencies (Metzger et al. 2019). In contrast, at LOFAR frequencies of $110 - 188$ MHz we see $> 10\times$ higher fluences compared to bursts detected by CHIME/FRB at $400 - 800$ MHz (Table 1). Similarly, the detection of 110-MHz emission also places constraints on magnetospheric emission heights and models, e.g., the curvature radiation model (Kumar et al. 2017).

4.2. *Spectro-temporal and polarimetric behaviour*

The spectro-temporal properties of the 17 CHIME/FRB bursts presented here (Figure 8) are consistent with those of the 38 CHIME/FRB bursts previously presented in the literature. As such, we do not discuss their properties in detail.

The five new uGMRT bursts (detected at $200 - 450\,\mathrm{MHz}$) complement the 15 previously detected at $550 - 750\,\mathrm{MHz}$ (Marthi et al. 2020). Of the new uGMRT bursts, G5 (Figures 6 and 7) has the most intriguing spectro-temporal properties, showing sub-structures that do not completely match the typical 'sad trombone' downward-drift features seen from repeaters (e.g., Hessels et al. 2019). A similar morphology has been observed in some bursts from FRB 20121102A (Caleb et al. 2020; Hilmarsson et al. 2020) and FRB 20180916B (Chawla et al. 2020). However, it is unclear whether these represent drifting sub-bursts within a single burst envelope, or a closely spaced set of separate bursts peaking at different frequencies, and then each individually drifting downwards in frequency. The short-timescale sub-structure of burst G5 also allows us to better investigate possible DM variations (as we discuss in the next sub-section).

The 18 LOFAR bursts constitute our first view of FRB emission below 300 MHz. These bursts have large widths (40 to 160 ms; Table 1) compared to other FRBs in general (e.g., Figure 13 in Petroff et al. 2019), and compared to FRB 20180916B at high frequency (Nimmo et al. 2020). This broadening is not due to dispersion smearing (see §2.1 and the coherently dedispersed waterfalls in Figure 3). For comparison, the typical burst width at 1.7 GHz is $\sim 2 - 3\,\mathrm{ms}$, and burst sub-structure has been detected on a wide range of timescales, down to $\sim 3 - 4\,\mu\mathrm{s}$ (Nimmo et al. 2020). It is not completely clear whether the larger burst widths at lower frequencies are simply due to scattering (extrinsic multi-path propagation through the intervening material), or whether they reflect an intrinsic aspect of the emission process — like the 'sad trombone' effect seen from FRB 20180916B and other repeaters, where the sub-burst drift to later times increases towards lower frequencies (Hessels et al. 2019).

Previously, Marcote et al. (2020) estimated a scattering time of $2.7\,\mu\mathrm{s}$ at 1.7 GHz, and Chawla et al. (2020) constrained the scattering time to be $< 1.7\,\mathrm{ms}$ at 350 MHz (this is compatible with the higher-frequency measurement). For a scattering time that scales with frequency as $\tau_{\mathrm{scatt}} \propto \nu^{-4}$, the effect is $30\times$ larger at 150 MHz compared to 350 MHz and $100\times$ larger at 110 MHz. Based on the measured scattering time of Marcote et al. (2020), we expect a scattering time of $\sim 40\,\mathrm{ms}$ at 150 MHz, for a ν^{-4} scaling. This matches well with the modeled scattering times of the high-S/N

complex voltage data bursts CV1 and CV4 (Table 2). Regardless of modeling, bursts I14 and CV4 are the brightest detected bursts in the top- and bottom-half of the LOFAR HBA band, respectively, and both show clear asymmetric tails (as do other high-S/N bursts). Their measured widths of $54\pm2\,\mathrm{ms}$ at 161 MHz (I14) and $158 \pm 7\,\mathrm{ms}$ at 116 MHz (CV4) are also consistent with what one would predict by extrapolating from the scattering measurement of Marcote et al. (2020). However, the LOFAR bursts may be additionally broadened by a poorly resolved 'sad trombone' effect as well. The drift towards later times increases towards lower frequencies (Hessels et al. 2019; Josephy et al. 2019) and, based on FRB 20180916B observations in the CHIME/FRB band (PR3), could be $\sim 10\,\mathrm{ms}$ per $\sim 50\,\mathrm{MHz}$ at LOFAR frequencies. We also note that many bursts from FRB 20121102A show asymmetric burst profiles regardless of scattering (Hessels et al. 2019). Additional LOFAR observations spanning a wide range of epochs can constrain whether the scattering time varies systematically, as is seen from the Crab pulsar (Driessen et al. 2019). Our burst detections spanning ~ 10 months show no obvious evidence for this, however.

The detection of FRB 20180916B, with DM $\sim 350\,\mathrm{pc\,cm^{-3}}$, in the LOFAR HBA band contrasts with results from the LOFAR HBA ($110 - 188\,\mathrm{MHz}$) census of slow and millisecond pulsars (Bilous et al. 2016; Kondratiev et al. 2016), as well as the new and known pulsars detected in the LOFAR Tied-Array All-Sky survey (LOTAAS; Sanidas et al. 2019). None of these observations detect Galactic pulsars with DM $\gtrsim 220\,\mathrm{pc\,cm^{-3}}$. The absence of LOFAR pulsar detections above this limit is consistent (Sanidas et al. 2019) with predictions from the Galactic scattering relations derived by Bhat et al. (2004) and Geyer et al. (2017). Indeed, extragalactic FRBs are often significantly less scattered than Galactic pulsars of comparable DM (see, e.g., Figure 16 of Cordes & Chatterjee 2019, though note that FRB 20180916B has low Galactic latitude $b = 3.7°$).

In previous, simultaneous LOFAR HBA, GBT and CHIME/FRB observations, bursts were detected at $> 300\,\mathrm{MHz}$, but not at $110 - 188\,\mathrm{MHz}$ (Chawla et al. 2020). Of the CHIME/FRB, uGMRT and LOFAR observations presented here, the arrival times of five CHIME/FRB bursts from CHIME/FRB Collaboration et al. (2020a) overlap with LOFAR observations, of which three have been presented in Chawla et al. (2020). None of these bursts have counterparts in the $110 - 188\,\mathrm{MHz}$ band of LOFAR. Similarly, Pearlman et al. (2020) used simultaneous CHIME/FRB and Deep Space Network (DSN) 70-m dish observations to demonstrate a burst detection in the CHIME/FRB band, but none at 2.3 GHz or 8.4 GHz.

Clearly, FRB 20180916B bursts have a low instantaneous bandwidth, as has been seen for FRB 20121102A (Gourdji et al. 2019; Majid et al. 2020) and beautifully demonstrated for FRB 20190711A (Kumar et al. 2021). The LOFAR HBA bursts we present here show bandwidths of $20 - 50$ MHz, and are consistent with an emerging picture in which repeating FRB bursts have typical fractional bandwidths (BW/$\nu_{\rm obs}$) of $\sim 20\%$ (e.g., CHIME/FRB Collaboration et al. 2019a; Gourdji et al. 2019). The large sample of FRB 20180916B bursts that are now available from $110 - 1700$ MHz could also be stacked to determine an average spectral index — though that requires careful consideration of CHIME/FRB beam effects and other instrumental biases/selection effects, and is beyond the scope of this work.

Lastly, for three LOFAR HBA bursts with full polarimetric data available, we have measured the linear and circular polarization fractions (Figure 4). We find broad similarity to the polarimetric properties measured for FRB 20180916B bursts at 350 MHz (Chawla et al. 2020) and 1.7 GHz (Nimmo et al. 2020): i.e., high linear polarization fraction, with flat polarization angle during the burst, and negligible circular polarization fraction, persists from $130 - 1700$ MHz — almost four octaves in radio frequency. For the low-frequency Burst CV4, the lower linear polarization fraction is likely due to scattering, though investigations are ongoing to determine whether this could be the result of Faraday conversion (Gruzinov & Levin 2019; Vedantham & Ravi 2019). The remarkably similar polarimetric burst profiles across a wide range of radio frequencies is dissimilar to what is seen in some pulsars (Noutsos et al. 2015), and provides a novel constraint on FRB emission theory.

4.3. DM and RM variations

Despite the low frequencies of our LOFAR HBA burst detections, the large burst widths and likely presence of scattering make it difficult to precisely and accurately determine the burst DMs in order to investigate potential DM variability. For this reason, we have dedispersed all bursts in Figure 2 to a best-fit literature value of DM= 348.772 pc cm^{-3} (Nimmo et al. 2020). Previously, PR3 searched for DM variability, also as a function of FRB 20180916B's activity phase. Using structure-optimized DMs (Hessels et al. 2019) from four bursts detected using the CHIME/FRB baseband capture system, they found no DM variations with magnitude $\gtrsim 0.1$ pc cm^{-3}.

Using three high-S/N bursts detected at $550 - 750$ MHz with uGMRT, and searching for a DM that maximizes burst sub-structure (Hessels et al.

2019), Marthi et al. (2020) also found no evidence for large DM variations. Their strongest constraint, DM $= 348.8 \pm 0.1$ pc cm^{-3} (for their burst 11), is also consistent with the DM= 348.772 pc cm^{-3} (Nimmo et al. 2020) value we use throughout this paper. Optimizing the sub-structure of burst G5 (Figure 7), we find DM = $349.5(1)$ pc cm^{-3}. However, as we noted in the previous sub-section, there is some ambiguity in the interpretation of the burst structure of G5. Nevertheless, any DM variations are constrained to be $\lesssim 1$ pc cm^{-3}.

The LOFAR HBA burst detections do provide precise RM values. Comparing with previous GBT and CHIME/FRB measurements (CHIME/FRB Collaboration et al. 2019a; Chawla et al. 2020), and correcting for the variable RM contribution from the Earth's ionosphere, we find that FRB 20180916B shows significant variations at the level of $\sim 2 - 3$ rad m^{-2} ($\sim 2\%$ fractional; though the variable component of the RM may be much lower than the total line-of-sight RM, in which case the fractional variations could be much larger). With only seven measurements in hand, it is not yet clear whether the observed RM is correlated with the activity phase of the source, or varies stochastically (Figure 5). Alternatively, the RM (and DM) could also depend on radio frequency, e.g., if there is a frequency dependence to the location of the emission region.

4.4. Observed activity

A revised analysis of the 38 previously published and 17 newly presented CHIME/FRB bursts — spanning two years, and thus 45 activity cycles, from 2018 September 16 until 2020 September 19 — provides a refined source activity period of $P_{\rm act} = 16.33 \pm 0.12$ days using the same methodology as in PR3. This is consistent with the previously published determination of $P_{\rm act} = 16.35 \pm 0.15$ days. The refined activity window is 5.2 days, as compared to the 5.4-day window that was measured using only 38 events.

Folding all bursts modulo $P_{\rm act}$, we see that the 18 LOFAR HBA bursts are systematically delayed in activity phase, by $\sim$three days (0.2 cycles), compared to the 55 CHIME/FRB bursts (Figure 9). As we show in Figure 10, this effect is not simply a reflection of the observational exposure. LOFAR HBA bursts have been detected in four activity cycles, namely Cycles 20, 21, 35, 37. Though the number of observations and bursts per cycle is low, these are consistent with the delayed activity being a time-invariant effect. Cycle 37 provides the best single-cycle observational coverage and burst sample between CHIME/FRB and LOFAR (Figure 1), and is also consistent with the overall picture one obtains by summing over all activity cycles. An ongoing campaign

of NenuFAR, LOFAR HBA and Effelsberg observations will better characterize this frequency-dependent activity, and determine whether the low-frequency activity window has a larger duty cycle, or not. A larger burst sample can also, in principle, determine the functional form of the activity delay with frequency, e.g. whether the delay as a function of frequency is linear or quadratic.

Higher-frequency detections of FRB 20180916B at L-band seem to preferentially arrive at the start of the CHIME/FRB-derived activity window (PR3, Aggarwal et al. 2020). In follow-up observations of repeaters with periodic activity it thus seems wise to cover a broad window and not only the peak of activity derived at a different frequency.

4.5. A self-consistent model for FRB 20180916B

We now consider what models can naturally accommodate the wealth of observational facts available for FRB 20180916B.

Recently, Tendulkar et al. (2020) used *Hubble Space Telescope* and Gran Telescopio Canarias observations to demonstrate that FRB 20180916B is significantly offset with respect to nearby star-forming regions in its host galaxy. Assuming it is a neutron star formed in one of these regions, as opposed to *in situ*, it is more likely to be an old ($100 \, \mathrm{kyr}$ to $10 \, \mathrm{Myr}$) source. Coupled with the observed 16.3-day activity period, this led Tendulkar et al. (2020) to suggest that the system could be a high-mass X-ray binary (HMXB), where the bursts are possibly generated through an interaction between the companion wind and neutron star magnetosphere (sometimes called a 'cosmic comb' model, e.g. Zhang 2017; Ioka & Zhang 2020). Furthermore, the detection of a wide range (factor ~ 1000) of emission timescales and microsecond structure in some FRB 20180916B bursts (Nimmo et al. 2020) is more naturally explained in terms of magnetospheric emission models, as opposed to those that invoke emission in a relativistic shock far from the neutron star.

HMXBs are relatively common: there are roughly 200 known in the Milky Way (Coleiro & Chaty 2013; Walter et al. 2015). Furthermore, studies find that binary interaction dominates the evolution of massive stars (Sana et al. 2012), and hence highly magnetized neutron stars in such binaries should not be particularly rare. In fact, HMXBs are arguably *too* abundant to explain repeating FRBs, unless one invokes particular evolutionary stages, sporadic emission episodes, and/or viewing geometry to explain the lack of radio burst detections from Galactic HMXBs, as we discuss further below.

The detection of low-frequency bursts with no simultaneous high-frequency emission (Pearlman et al. 2020),

strongly challenges models in which the 16.3-day observed periodicity is the result of absorption by the companion wind (Lyutikov et al. 2020). Rather, our LOFAR HBA detections and the lack of any observed DM variations, with $\Delta \mathrm{DM} \lesssim 0.1 \, \mathrm{pc} \, \mathrm{cm}^{-3}$ throughout the active window (PR3), suggest that we have a relatively clean line-of-sight to the burst source itself. Nonetheless, the observed RM variations of FRB 20180916B are atypical and not seen from isolated Galactic pulsars; they suggest that it is in a special local environment.

It is interesting to compare FRB 20180916B with known radio pulsar/OB-star binary systems. One example is the Small Magellanic Cloud (SMC) radio pulsar/B1V-companion binary system PSR J0045$-$7319. In this 51-day highly eccentric binary, at periastron and apastron, the pulsar approaches to within four and 34 B-star radii from the companion, respectively, probing very different regions of the stellar wind. Yet Kaspi et al. (1996) found an upper limit on DM variations $< 0.9 \, \mathrm{pc} \, \mathrm{cm}^{-3}$, yielding a strong constraint on the stellar wind, $< 10^{-11} \, \mathrm{M_\odot} \, \mathrm{yr}^{-1}$. Given the low metallicity of the SMC, a B-star with so weak a wind is not unexpected.

In a similar way, the lack of large observed DM variations (i.e., $\Delta \mathrm{DM} \lesssim 1 \, \mathrm{pc} \, \mathrm{cm}^{-3}$) from FRB 20180916B may not be problematic for a massive star binary model. Based on population synthesis arguments, Zhang & Gao (2020) argue that B-type stars would be the most likely companions to FRB binary sources. If the putative FRB 20180916B orbit is not very eccentric, the variation in pulsar/companion distance with orbital phase may not be large. This, together with a relatively weak companion wind, may make DM variations hard to observe. On the other hand, the Galactic eccentric radio pulsar/OB-star binary PSR J1740$-$3052 does show DM variations of order $\sim 2 \, \mathrm{pc} \, \mathrm{cm}^{-3}$ near periastron in its 231-day orbit; these imply a mass-loss rate on the order of $10^{-9} \, \mathrm{M_\odot} \, \mathrm{yr}^{-1}$, still low for a Galactic O or early B star (Madsen et al. 2012). For similar strength wind, given the 16.3-day orbital period and hence closer pulsar/companion distance, the CHIME/FRB-active window would have to occur near apastron, or the orbit would have to be fairly circular to avoid detectable DM changes. Similarly, the Galactic highly eccentric 1237-day radio pulsar/Be-star binary PSR B1259$-$63 shows large DM, RM and scattering-time variations in the ~ 50 days near periastron ($\Delta \mathrm{DM} \simeq 6 - 8 \, \mathrm{pc} \, \mathrm{cm}^{-3}$, $\Delta \mathrm{RM} \simeq 6000 \, \mathrm{rad} \, \mathrm{m}^{-2}$, and increased scattering such that 1.5-GHz pulse profiles become unobservable for this 48-ms pulsar), though these are likely due to the presence of a circumstellar disk through which the pulsar passes (Johnston et al. 1992, 1996, 2005). An emission-

line star in the FRB 20180916B system seems implausible, because of the shorter orbital period, hence more compact orbit size and pulsar/star separation, together with the constraints on DM variations, absence of sizable RM variations, and given our new low-frequency detections which rule out large scattering times and which are offset in phase.

In the context of interacting binary models (Lyutikov et al. 2020; Ioka & Zhang 2020; Popov 2020; Du et al. 2021), the FRBs may be produced by a highly magnetized neutron star whose magnetosphere is 'combed' by the ionized wind of a massive companion star. Such interaction could lead to magnetic reconnection events, which have been proposed as a source of FRBs (Lyutikov & Popov 2020). The bursts may only be visible within a funnel where the neutron star's wind shields against the companion's wind, which is otherwise opaque to induced Compton or Raman scattering for FRB emission (Ioka & Zhang 2020, see their Figure 1). Windows of observable burst activity, lasting for $\sim 4-5$ days in the case of FRB 20180916B, then correspond to when this funnel, and the induced magnetic tail of the neutron star, are pointed towards Earth. This special viewing geometry could also, in principle, explain why Galactic HMXBs are not known to be prolific sources of bright radio bursts.

The funnel and magnetic tail can also be swept back by orbital motion. Wang et al. (2019) and Lyutikov (2020) discuss a radius-to-frequency mapping model to explain the 'sad trombone' effect seen from repeating FRBs on timescales of milliseconds (Hessels et al. 2019). If the radio emission frequency of bursts indeed scales with distance from the central source, where the magnetic field strength and plasma density are lower at larger distances, then this could plausibly also explain why the LOFAR HBA bursts we have observed are delayed in activity phase with respect to those seen at higher frequencies by CHIME/FRB. In such a toy model, the LOFAR bursts would originate at larger distances from the neutron star, in a swept-back magnetic tail.

While a model in which FRB 20180916B is a highly magnetized neutron star in an interacting HMXB system can plausibly explain all the observed phenomena to date, several authors have argued that the 16.3-day activity period of FRB 20180916B is the rotational period (Beniamini et al. 2020), or precession period (Levin et al. 2020; Sob'yanin 2020; Yang & Zou 2020; Zanazzi & Lai 2020), of an isolated magnetar. Tendulkar et al. (2020) have argued against a young source, and the consistent polarization position angle *between* bursts (Nimmo et al. 2020) sets significant constraints on precession models.

Nonetheless, in the context of these non-binary models, the frequency dependence of the observed activity could also be interpreted as a radius-to-frequency mapping effect in an emission cone that is slowly sweeping past the line of sight and is perhaps swept backwards at higher altitudes.

Lastly, we note that FRB 20180916B and FRB 20121102A, the two best-studied repeaters, share remarkably similar phenomenology (see §1) — despite the fact that FRB 20121102A is hosted in a much less massive dwarf galaxy and is coincident with a compact, persistent radio source. They are almost certainly of a similar physical origin, though FRB 20121102A may be in the vicinity of an accreting massive black hole (Michilli et al. 2018). Such a Galactic-center-like environment, coupled with its very low Galactic latitude, may explain why — unlike FRB 20180916B ($b = 3.7°$) — FRB 20121102A ($b = -0.2°$) has only been detected once at radio frequencies $< 1\,\mathrm{GHz}$ (Josephy et al. 2019).

5. CONCLUSIONS

Using LOFAR observations in the $110 - 188$-MHz band, we have detected 18 bursts from FRB 20180916B, which are the first FRBs to be detected below 300 MHz. Since some of the detected bursts are bright down to the lowest-observed frequency of 110 MHz, it is likely that FRB 20180916B emission extends to even lower frequencies — though scattering ($\sim 50\,\mathrm{ms}$ at $150\,\mathrm{MHz}$) and sky background temperature will limit their detectability unless the fluences also increase and compensate for these effects. We are now actively searching for $< 100\,\mathrm{MHz}$ emission using coordinated LOFAR and NenuFAR observations. The discovery of FRB emission in the $110 - 188$-MHz band also gives new impetus to searches for additional sources in this band.

LOFAR polarimetric data demonstrate consistency with the properties previously presented at higher radio frequencies of $300 - 1700\,\mathrm{MHz}$. The LOFAR bursts, combined with previous measurements, also show $2 - 3\,\mathrm{rad\,m^{-2}}$ RM variations. One highly structured burst from the five new detections we presented from uGMRT ($200 - 450\,\mathrm{MHz}$) leaves room for small but significant DM variations ($\lesssim 1\,\mathrm{pc\,cm^{-3}}$) depending on the interpretation of its burst morphology.

Lastly, we also presented 17 new CHIME/FRB bursts detected at $400-800\,\mathrm{MHz}$. For five CHIME/FRB bursts with overlapping LOFAR observations, we detect no emission in the LOFAR $110-188$-MHz band. This again emphasises the narrow-band nature of repeating FRB bursts, as previously discussed for a number of sources in the literature.

Using the full available sample of 55 CHIME/FRB bursts, spanning two years, we confirm that FRB 20180916B is periodically active, with a refined period of 16.33±0.12 days over the 45 cycles observed to date. Comparing with the 55 CHIME/FRB bursts, we show that the LOFAR bursts arrive systematically later in the 16.33-day activity cycle of the source. We find a ∼three day (0.2 cycle) shift across the two octaves in radio frequency from 600 MHz to 150 MHz.

We interpret these results in the context of the rich set of observational facts that are known about the FRB 20180916B burst properties and the local environment in its massive host galaxy. We discuss how a model in which FRB 20180916B is an interacting neutron-star HMXB system can account for all the observational results to date.

REFERENCES

Agarwal, D., Aggarwal, K., Burke-Spolaor, S., Lorimer, D. R., & Garver-Daniels, N. 2020, MNRAS, 497, 1661, doi: 10.1093/mnras/staa1856

Aggarwal, K., Law, C. J., Burke-Spolaor, S., et al. 2020, Research Notes of the American Astronomical Society, 4, 94, doi: 10.3847/2515-5172/ab9f33

Astropy Collaboration, Robitaille, T. P., Tollerud, E. J., et al. 2013, A&A, 558, A33, doi: 10.1051/0004-6361/201322068

Astropy Collaboration, Price-Whelan, A. M., Sipőcz, B. M., et al. 2018, AJ, 156, 123, doi: 10.3847/1538-3881/aabc4f

Barsdell, B. R., Bailes, M., Barnes, D. G., & Fluke, C. J. 2012, MNRAS, 422, 379, doi: 10.1111/j.1365-2966.2012.20622.x

Bassa, C. G., Pleunis, Z., & Hessels, J. W. T. 2017a, Astronomy and Computing, 18, 40, doi: 10.1016/j.ascom.2017.01.004

Bassa, C. G., Pleunis, Z., Hessels, J. W. T., et al. 2017b, ApJL, 846, L20, doi: 10.3847/2041-8213/aa8400

Beniamini, P., Wadiasingh, Z., & Metzger, B. D. 2020, MNRAS, 496, 3390, doi: 10.1093/mnras/staa1783

Bhat, N. D. R., Cordes, J. M., Camilo, F., Nice, D. J., & Lorimer, D. R. 2004, ApJ, 605, 759, doi: 10.1086/382680

Bilous, A. V., Kondratiev, V. I., Kramer, M., et al. 2016, A&A, 591, A134, doi: 10.1051/0004-6361/201527702

Bochenek, C. D., Ravi, V., Belov, K. V., et al. 2020, Nature, 587, 59, doi: 10.1038/s41586-020-2872-x

Bondonneau, L., Grießmeier, J. M., Theureau, G., et al. 2020, arXiv e-prints, arXiv:2009.02076. https://arxiv.org/abs/2009.02076

Brentjens, M. A., & de Bruyn, A. G. 2005, A&A, 441, 1217, doi: 10.1051/0004-6361:20052990

Broekema, P. C., Mol, J. J. D., Nijboer, R., et al. 2018, Astronomy and Computing, 23, 180, doi: 10.1016/j.ascom.2018.04.006

Burn, B. J. 1966, MNRAS, 133, 67, doi: 10.1093/mnras/133.1.67

Caleb, M., Stappers, B. W., Abbott, T. D., et al. 2020, MNRAS, 496, 4565, doi: 10.1093/mnras/staa1791

Chawla, P., Andersen, B. C., Bhardwaj, M., et al. 2020, ApJL, 896, L41, doi: 10.3847/2041-8213/ab96bf

CHIME/FRB Collaboration. 2018, ApJ, 863, 48, doi: 10.3847/1538-4357/aad188

CHIME/FRB Collaboration, Andersen, B. C., Bandura, K., et al. 2019a, ApJL, 885, L24, doi: 10.3847/2041-8213/ab4a80

CHIME/FRB Collaboration, Amiri, M., Bandura, K., et al. 2019b, Nature, 566, 235, doi: 10.1038/s41586-018-0864-x

CHIME/FRB Collaboration, Amiri, M., Andersen, B. C., et al. 2020a, Nature, 582, 351, doi: 10.1038/s41586-020-2398-2

CHIME/FRB Collaboration, Andersen, B. C., Bandura, K. M., Bhardwaj, M., et al. 2020b, Nature, 587, 54, doi: 10.1038/s41586-020-2863-y

Cho, H., Macquart, J.-P., Shannon, R. M., et al. 2020, ApJL, 891, L38, doi: 10.3847/2041-8213/ab7824

Coenen, T., van Leeuwen, J., Hessels, J. W. T., et al. 2014, A&A, 570, A60, doi: 10.1051/0004-6361/201424495

Coleiro, A., & Chaty, S. 2013, ApJ, 764, 185, doi: 10.1088/0004-637X/764/2/185

Colgate, S. A., & Noerdlinger, P. D. 1971, ApJ, 165, 509, doi: 10.1086/150918

Condon, J. J., & Ransom, S. M. 2016, Essential Radio Astronomy (Princeton University Press)

Cordes, J. M., & Chatterjee, S. 2019, ARA&A, 57, 417, doi: 10.1146/annurev-astro-091918-104501

Cruces, M., Spitler, L. G., Scholz, P., et al. 2021, MNRAS, 500, 448, doi: 10.1093/mnras/staa3223

Day, C. K., Deller, A. T., Shannon, R. M., et al. 2020, MNRAS, 497, 3335, doi: 10.1093/mnras/staa2138

Driessen, L. N., Janssen, G. H., Bassa, C. G., Stappers, B. W., & Stinebring, D. R. 2019, MNRAS, 483, 1224, doi: 10.1093/mnras/sty3192

Du, S., Wang, W., Wu, X., & Xu, R. 2021, MNRAS, 500, 4678, doi: 10.1093/mnras/staa3527

Farah, W., Flynn, C., Bailes, M., et al. 2018, MNRAS, 478, 1209, doi: 10.1093/mnras/sty1122

Fonseca, E., Andersen, B. C., Bhardwaj, M., et al. 2020, ApJL, 891, L6, doi: 10.3847/2041-8213/ab7208

Foreman-Mackey, D., Hogg, D. W., Lang, D., & Goodman, J. 2013, PASP, 125, 306, doi: 10.1086/670067

Gajjar, V., Siemion, A. P. V., Price, D. C., et al. 2018, ApJ, 863, 2, doi: 10.3847/1538-4357/aad005

Geyer, M., Karastergiou, A., Kondratiev, V. I., et al. 2017, MNRAS, 470, 2659, doi: 10.1093/mnras/stx1151

Gourdji, K., Michilli, D., Spitler, L. G., et al. 2019, ApJL, 877, L19, doi: 10.3847/2041-8213/ab1f8a

Gruzinov, A., & Levin, Y. 2019, ApJ, 876, 74, doi: 10.3847/1538-4357/ab0fa3

Gupta, Y., Ajithkumar, B., Kale, H. S., et al. 2017, Current Science, 113, 707

Hardy, L. K., Dhillon, V. S., Spitler, L. G., et al. 2017, MNRAS, 472, 2800, doi: 10.1093/mnras/stx2153

Harris, C. R., Millman, K. J., van der Walt, S. J., et al. 2020, Nature, 585, 357, doi: 10.1038/s41586-020-2649-2

Hassall, T. E., Stappers, B. W., Hessels, J. W. T., et al. 2012, A&A, 543, A66, doi: 10.1051/0004-6361/201218970

22

Heald, G. 2009, in IAU Symposium, Vol. 259, Cosmic Magnetic Fields: From Planets, to Stars and Galaxies, ed. K. G. Strassmeier, A. G. Kosovichev, & J. E. Beckman, 591–602, doi: 10.1017/S1743921309031421

Hessels, J. W. T., Spitler, L. G., Seymour, A. D., et al. 2019, ApJL, 876, L23, doi: 10.3847/2041-8213/ab13ae

Hewish, A., Bell, S. J., Pilkington, J. D. H., Scott, P. F., & Collins, R. A. 1968, Nature, 217, 709, doi: 10.1038/217709a0

Hilmarsson, G. H., Michilli, D., Spitler, L. G., et al. 2020, arXiv e-prints, arXiv:2009.12135. https://arxiv.org/abs/2009.12135

Hotan, A. W., van Straten, W., & Manchester, R. N. 2004, PASA, 21, 302, doi: 10.1071/AS04022

Houben, L. J. M., Spitler, L. G., ter Veen, S., et al. 2019, A&A, 623, A42, doi: 10.1051/0004-6361/201833875

Hunter, J. D. 2007, Computing in Science & Engineering, 9, 90, doi: 10.1109/MCSE.2007.55

Ioka, K., & Zhang, B. 2020, ApJL, 893, L26, doi: 10.3847/2041-8213/ab83fb

Johnston, S., Ball, L., Wang, N., & Manchester, R. N. 2005, MNRAS, 358, 1069, doi: 10.1111/j.1365-2966.2005.08854.x

Johnston, S., Manchester, R. N., Lyne, A. G., et al. 1992, ApJL, 387, L37, doi: 10.1086/186300

—. 1996, MNRAS, 279, 1026, doi: 10.1093/mnras/279.3.1026

Jones, E., Oliphant, T., Peterson, P., et al. 2001–, SciPy: Open source scientific tools for Python. http://www.scipy.org/

Josephy, A., Chawla, P., Fonseca, E., et al. 2019, ApJL, 882, L18, doi: 10.3847/2041-8213/ab2c00

Karastergiou, A., Chennamangalam, J., Armour, W., et al. 2015, MNRAS, 452, 1254, doi: 10.1093/mnras/stv1306

Kaspi, V. M., Tauris, T. M., & Manchester, R. N. 1996, ApJ, 459, 717, doi: 10.1086/176936

Kirsten, F., Snelders, M. P., Jenkins, M., et al. 2020, Nature Astronomy, doi: 10.1038/s41550-020-01246-3

Kondratiev, V. I., Verbiest, J. P. W., Hessels, J. W. T., et al. 2016, A&A, 585, A128, doi: 10.1051/0004-6361/201527178

Kulkarni, S. R. 2020, arXiv e-prints, arXiv:2007.02886. https://arxiv.org/abs/2007.02886

Kumar, P., Lu, W., & Bhattacharya, M. 2017, MNRAS, 468, 2726, doi: 10.1093/mnras/stx665

Kumar, P., Shannon, R. M., Flynn, C., et al. 2021, MNRAS, 500, 2525, doi: 10.1093/mnras/staa3436

Law, C. J., Abruzzo, M. W., Bassa, C. G., et al. 2017, ApJ, 850, 76, doi: 10.3847/1538-4357/aa9700

Levin, Y., Beloborodov, A. M., & Bransgrove, A. 2020, ApJL, 895, L30, doi: 10.3847/2041-8213/ab8c4c

Lorimer, D. R., Bailes, M., McLaughlin, M. A., Narkevic, D. J., & Crawford, F. 2007, Science, 318, 777, doi: 10.1126/science.1147532

Luo, R., Wang, B. J., Men, Y. P., et al. 2020, Nature, 586, 693, doi: 10.1038/s41586-020-2827-2

Lyutikov, M. 2020, ApJ, 889, 135, doi: 10.3847/1538-4357/ab55de

Lyutikov, M., Barkov, M. V., & Giannios, D. 2020, ApJL, 893, L39, doi: 10.3847/2041-8213/ab87a4

Lyutikov, M., & Popov, S. 2020, arXiv e-prints, arXiv:2005.05093. https://arxiv.org/abs/2005.05093

Madsen, E. C., Stairs, I. H., Kramer, M., et al. 2012, MNRAS, 425, 2378, doi: 10.1111/j.1365-2966.2012.21691.x

Majid, W. A., Pearlman, A. B., Nimmo, K., et al. 2020, ApJL, 897, L4, doi: 10.3847/2041-8213/ab9a4a

Manchester, R. N., & Taylor, J. H. 1972, Astrophys. Lett., 10, 67

Marcote, B., Nimmo, K., Hessels, J. W. T., et al. 2020, Nature, 577, 190, doi: 10.1038/s41586-019-1866-z

Marthi, V. R., Gautam, T., Li, D. Z., et al. 2020, MNRAS, 499, L16, doi: 10.1093/mnrasl/slaa148

Mereghetti, S., Savchenko, V., Ferrigno, C., et al. 2020, ApJL, 898, L29, doi: 10.3847/2041-8213/aba2cf

Metzger, B. D., Margalit, B., & Sironi, L. 2019, MNRAS, 485, 4091, doi: 10.1093/mnras/stz700

Michilli, D., Seymour, A., Hessels, J. W. T., et al. 2018, Nature, 553, 182, doi: 10.1038/nature25149

Nimmo, K., Hessels, J. W. T., Keimpema, A., et al. 2020, arXiv e-prints, arXiv:2010.05800. https://arxiv.org/abs/2010.05800

Noutsos, A., Sobey, C., Kondratiev, V. I., et al. 2015, A&A, 576, A62, doi: 10.1051/0004-6361/201425186

Parent, E., Chawla, P., Kaspi, V. M., et al. 2020, ApJ, 904, 92, doi: 10.3847/1538-4357/abbdf6

Pastor-Marazuela, I., Connor, L., van Leeuwen, J., et al. 2020, *submitted*

Pearlman, A. B., Majid, W. A., Prince, T. A., et al. 2020, arXiv e-prints, arXiv:2009.13559. https://arxiv.org/abs/2009.13559

Petroff, E., Hessels, J. W. T., & Lorimer, D. R. 2019, A&A Rv, 27, 4, doi: 10.1007/s00159-019-0116-6

Petroff, E., Johnston, S., Keane, E. F., et al. 2015, MNRAS, 454, 457, doi: 10.1093/mnras/stv1953

Phinney, S., & Taylor, J. H. 1979, Nature, 277, 117, doi: 10.1038/277117a0

Pilia, M., Burgay, M., Possenti, A., et al. 2020, ApJL, 896, L40, doi: 10.3847/2041-8213/ab96c0

Piro, A. L. 2016, ApJL, 824, L32,
doi: 10.3847/2041-8205/824/2/L32

Platts, E., Weltman, A., Walters, A., et al. 2019, PhR, 821,
1, doi: 10.1016/j.physrep.2019.06.003

Popov, S. B. 2020, Research Notes of the American
Astronomical Society, 4, 98,
doi: 10.3847/2515-5172/aba0af

Purcell, C. R., Van Eck, C. L., West, J., Sun, X. H., &
Gaensler, B. M. 2020, RM-Tools: Rotation measure (RM)
synthesis and Stokes QU-fitting.
http://ascl.net/2005.003

Rajwade, K. M., Mickaliger, M. B., Stappers, B. W., et al.
2020, MNRAS, 495, 3551, doi: 10.1093/mnras/staa1237

Ransom, S. M. 2001, PhD thesis, Harvard University

Ransom, S. M., Eikenberry, S. S., & Middleditch, J. 2002,
AJ, 124, 1788, doi: 10.1086/342285

Reddy, S. H., Kudale, S., Gokhale, U., et al. 2017, Journal
of Astronomical Instrumentation, 6, 1641011,
doi: 10.1142/S2251171716410117

Rowlinson, A., Bell, M. E., Murphy, T., et al. 2016,
MNRAS, 458, 3506, doi: 10.1093/mnras/stw451

Sana, H., de Mink, S. E., de Koter, A., et al. 2012, Science,
337, 444, doi: 10.1126/science.1223344

Sanidas, S., Cooper, S., Bassa, C. G., et al. 2019, A&A,
626, A104, doi: 10.1051/0004-6361/201935609

Scholz, P., Bogdanov, S., Hessels, J. W. T., et al. 2017,
ApJ, 846, 80, doi: 10.3847/1538-4357/aa8456

Scholz, P., Cook, A., Cruces, M., et al. 2020, ApJ, 901, 165,
doi: 10.3847/1538-4357/abb1a8

Seymour, A., Michilli, D., & Pleunis, Z. 2019, DM_phase:
Algorithm for correcting dispersion of radio signals.
http://ascl.net/1910.004

Shannon, R. M., Macquart, J. P., Bannister, K. W., et al.
2018, Nature, 562, 386, doi: 10.1038/s41586-018-0588-y

Sobey, C., Bilous, A. V., Grießmeier, J. M., et al. 2019,
MNRAS, 484, 3646, doi: 10.1093/mnras/stz214

Sob'yanin, D. N. 2020, MNRAS, 497, 1001,
doi: 10.1093/mnras/staa1976

Sokolowski, M., Bhat, N. D. R., Macquart, J. P., et al.
2018, ApJL, 867, L12, doi: 10.3847/2041-8213/aae58d

Sotomayor-Beltran, C., Sobey, C., Hessels, J. W. T., et al.
2013, A&A, 552, A58, doi: 10.1051/0004-6361/201220728

Spitler, L. G., Scholz, P., Hessels, J. W. T., et al. 2016,
Nature, 531, 202, doi: 10.1038/nature17168

Stappers, B. W., Hessels, J. W. T., Alexov, A., et al. 2011,
A&A, 530, A80, doi: 10.1051/0004-6361/201116681

Susobhanan, A., Maan, Y., Joshi, B. C., et al. 2020, arXiv
e-prints, arXiv:2007.02930.
https://arxiv.org/abs/2007.02930

Tendulkar, S. P., Gil de Paz, A., Kirichenko, A. Y., et al.
2020, arXiv e-prints, arXiv:2011.03257.
https://arxiv.org/abs/2011.03257

Tingay, S. J., Trott, C. M., Wayth, R. B., et al. 2015, AJ,
150, 199, doi: 10.1088/0004-6256/150/6/199

van Haarlem, M. P., Wise, M. W., Gunst, A. W., et al.
2013, A&A, 556, A2, doi: 10.1051/0004-6361/201220873

van Straten, W., & Bailes, M. 2011, PASA, 28, 1,
doi: 10.1071/AS10021

Vedantham, H. K., & Ravi, V. 2019, MNRAS, 485, L78,
doi: 10.1093/mnrasl/slz038

Walter, R., Lutovinov, A. A., Bozzo, E., & Tsygankov, S. S.
2015, A&A Rv, 23, 2, doi: 10.1007/s00159-015-0082-6

Wang, W., Zhang, B., Chen, X., & Xu, R. 2019, ApJL, 876,
L15, doi: 10.3847/2041-8213/ab1aab

Xue, M., Ord, S. M., Tremblay, S. E., et al. 2019, PASA,
36, e025, doi: 10.1017/pasa.2019.19

Yang, H., & Zou, Y.-C. 2020, ApJL, 893, L31,
doi: 10.3847/2041-8213/ab800f

Zanazzi, J. J., & Lai, D. 2020, ApJL, 892, L15,
doi: 10.3847/2041-8213/ab7cdd

Zhang, B. 2017, ApJL, 836, L32,
doi: 10.3847/2041-8213/aa5ded

Zhang, X., & Gao, H. 2020, MNRAS, 498, L1,
doi: 10.1093/mnrasl/slaa116

Zhang, Y. G., Gajjar, V., Foster, G., et al. 2018, ApJ, 866,
149, doi: 10.3847/1538-4357/aadf31